

## Article

# Experimental and Numerical Study of the Influence of Solar Radiation on the Surface Temperature Field of Low-Heat Concrete in a Pouring Block

Zhipeng Liang, Huawei Zhou \*, Chunju Zhao , Fang Wang and Yihong Zhou

School of Civil Engineering, Architecture & Environment, Hubei University of Technology, Wuhan 430068, China; liangzhipeng@hbut.edu.cn (Z.L.); zhaochunju@hbut.edu.cn (C.Z.); wangfang0235@163.com (F.W.); zhouyihong@hbut.edu.cn (Y.Z.)

\* Correspondence: zhouhuawei@hbut.edu.cn

**Abstract:** With the influence of intense solar radiation heat and the greater temperature difference between day and night, surface concrete with a drastic temperature change can easily experience a great nonlinear temperature difference, which increases the risk of early-age concrete cracking. In this study, a distributed optical fiber temperature sensing (DTS) system is used to monitor the surface temperature gradient of concrete in real time, and a solar radiation heat monitoring test is also carried out based on the Baihetan project. Based on this, a solar radiation loading model and a finite element model of a typical pouring block considering solar radiation are established. Combined with the measured temperature data and different calculation conditions, the surface temperature changes of medium-heat and low-heat concrete experiencing solar radiation are analyzed, and the temperature control effect of surface concrete with different surface insulation measures is further analyzed. The results show that the temperature variation of medium-heat concrete at the same depth is more obvious than that of low-heat concrete. Additionally, the temperature variation of low-heat concrete is noticeable within 20 cm of the top surface. In addition, in an intense solar radiation environment, covering the concrete with a 4- or 5-centimeter-thick polyethylene coil can effectively control the surface temperature gradient and maximum daily amplitude of low-heat concrete, and surface concrete cured by running water has a significant temperature control effect. Therefore, it is suggested that 22–24 °C water temperatures be used for water curing during periods of intense solar radiation during the day and a 4-centimeter-thick polyethylene coil be used for coverage at night. These study results have been employed in the Baihetan project to optimize the temperature control scheme of the pouring blocks.

**Keywords:** solar radiation heat; low-heat concrete; daily maximum variation; surface temperature gradient of a pouring block; temperature control scheme



**Citation:** Liang, Z.; Zhou, H.; Zhao, C.; Wang, F.; Zhou, Y. Experimental and Numerical Study of the Influence of Solar Radiation on the Surface Temperature Field of Low-Heat Concrete in a Pouring Block.

*Buildings* **2023**, *13*, 1519. <https://doi.org/10.3390/buildings13061519>

Academic Editors: Bo Yu, Sin Chi Kuok and Yang Zhang

Received: 11 May 2023

Revised: 9 June 2023

Accepted: 12 June 2023

Published: 13 June 2023



**Copyright:** © 2023 by the authors. Licensee MDPI, Basel, Switzerland. This article is an open access article distributed under the terms and conditions of the Creative Commons Attribution (CC BY) license (<https://creativecommons.org/licenses/by/4.0/>).

## 1. Introduction

In recent years, low-heat concrete has become the focus of attention in the field of hydraulic engineering due to its low hydration heat, high later strength, high durability, and high corrosion resistance compared to ordinary concrete [1–4]. The utilization of low-heat concrete is considered to be one of the most effective methods to decrease the thermal stresses and cracking risk in the dam concrete [5]. Low-heat concrete has the merits of low hydration heat, high strength, and good durability, which are beneficial for decreasing the temperature control stress of mass concrete and enhancing the crack resistance of concrete [6,7]. Low-heat concrete possesses better early crack resistance than ordinary concrete due to its lower shrinkage strain at an early age, and the hydration heat and adiabatic temperature rise of low-heat concrete are lower than those of ordinary concrete at all hydration ages. In addition, low-heat concrete has a more refined porous structure than ordinary concrete at late ages [5]. Researchers have systematically studied the performance

of low-heat concrete [8,9], and low-heat concrete was applied to the stilling pool of the Xiangjiaba project [10], the flood discharge tunnel of the Xiluodu project [11], and the diversion tunnel of the Baihetan project [12]. Additionally, low-heat concrete was used in the entire dam section of the Baihetan and Wudongde projects under construction in China, and applications of low-heat concrete are booming [13,14]. Ji et al. [15], Yang et al. [16], and Xin et al. [17] pointed out that the comprehensive performance of low-heat cement concrete is better than that of medium-heat cement's. Shi et al. [18] design lightweight thermal insulation mortar with improved thermal characteristics using glazed hollow beads and micro-encapsulated phase change materials. Peng et al. [4] investigated the composition of CTF and its influence on cement hydration, concrete temperature, and strength for the Wudongde dam project. However, the above two major projects are located in areas with strong solar radiation. The summer is hot, and the sun is strong. The highest temperature in the valley during the day is above 37 °C, the nighttime temperature is around 22 °C, and the temperature difference between day and night is above 10 °C. With the influences of strong solar radiation and the temperature difference between day and night, the surface temperature of a concrete block changes drastically, the internal concrete temperature changes slowly, and there may be a large temperature gradient from the inside to the outside, which causes large tensile stress. Due to the low early strength of low-heat concrete, the tensile stress is likely to exceed the tensile strength of the corresponding aged concrete, which induces cracks on the concrete surface, reduces the durability of the concrete structure, and may form serious penetrating cracks, which is disadvantageous to structural safety. Therefore, the key to ensuring the quality of dam temperature control is to perform the surface thermal insulation measures on low-heat concrete well before the high-temperature season.

For areas with strong solar radiation, it is the basis for the development of scientific and reasonable surface insulation measures to clarify the influence of solar radiation on the temperature state of concrete structures. In recent years, many scholars have studied the temperature state of concrete structures under the action of sunlight. Radiation can supply pore water with additional energy to change from the liquid to the vapor phase and increase evaporation. Radiation can cause the concrete surface temperature to rise above the air temperature, creating a vapor pressure deficiency and increasing evaporation [19–21]. Moelich et al. [19] investigated the influence of solar radiation on evaporation, concrete temperature, plastic shrinkage, and cracking. Wang et al. [22] carried out a temperature monitoring experiment and a numerical simulation of the orifice structure in an arch dam, considering solar radiation effects. Sheng et al. [23] investigated the non-uniform temperature distribution of the steel-concrete composite box girder-ballastless track system induced by the time-varying solar radiation. Li et al. [24] proposed that large temperature changes and strong solar radiation would hinder concrete temperature control and crack prevention. Zhu et al. [25] proposed that the seasonal variation in the solar azimuth angle will make the solar radiation absorbed by different regions of high arch dams vary greatly, which may lead to an uneven temperature distribution on the surface of high arch dams and then to adverse stress in the construction and operation of high arch dams. Chang et al. [26] calculated the influence of solar radiation on the temperature state of a roller compacted concrete (RCC) dam in the high-temperature season and determined that the calculated temperature field considering the influence of sunshine was closer to the actual temperature field. Huang et al. [27] calculated the influence of solar radiant heat on the temperature rise of RCC by simulation. Ren et al. [28] calculated the temperature field of a reinforced concrete pier under the action of sunlight. The surface temperature of a reinforced concrete pier under the action of solar radiation reached 52 °C. Oskae et al. [29] considered that solar radiant heat was the cause of the uneven temperature field of concrete bridges. Zhou et al. [30] simulated the surface temperature stress field for medium-heat concrete with the action of sunlight. They believed that the influence of solar radiant heat was very unfavorable for the crack resistance of early-age concrete. Su et al. [31] obtained the influence law of continuous sunshine on the temperature field of a diversion

wall according to an actual project. Zhou [32] and Zhao et al. [33] gave the temperature field distribution of a concrete box girder structure considering the influence of sunshine, and the solar radiant heat caused a large temperature difference between the upper and lower parts of the box girder structure. Soltani et al. [34] demonstrated that the influence of solar radiation on the simulation analysis of arch dams is reflected by an increase in the ambient temperature. Castilho et al. [35] calculated the solar radiation using the solar radiation calculation model and applied it to the finite element model as the third boundary condition, and the calculation results of the finite element analysis agreed well with the measured values.

The above research results provide a reference for the development of temperature control measures for roller-compacted concrete dams and bridges in a strong solar radiation environment. However, for a low-heat concrete dam project, the solar radiation absorption rate is different due to the different types of concrete. Therefore, the degree of influence of solar radiant heat on concrete must also be different. Additionally, the real temperature gradient of a low-heat concrete surface and the influence of solar radiation heat on the real temperature gradient of surface concrete lack experimental temperature monitoring research. At the same time, the real-time monitoring of the solar radiation heat on the surface of the concrete pouring block and the finite element simulation calculation based on the measured solar radiation intensity can truly restore the actual situation. On this basis, it is more accurate and reliable to determine the influence of different temperature control measures on the temperature field of the concrete pouring block.

In this research, a typical concrete block of Baihetan high arch dam with low-heat concrete is taken as the research object, a DTS system is used to monitor the surface concrete temperature gradient in real time, and a solar radiation monitoring test is carried out. Based on the measured concrete temperature data and meteorological data, the real thermal parameters of the dam in the high-temperature season are inverted, and the influence of solar radiant heat on the daily variation of the low-heat concrete temperature is analyzed. Meanwhile, a solar radiation loading model and a finite element model have been established. Combined with the measured temperature data and different calculation conditions, the surface temperature changes of medium and low-heat concrete under solar radiation are analyzed, and the temperature control effect of surface concrete with different surface insulation measures is further analyzed. Based on this, the feedback analysis of the surface temperature state of low-heat concrete with and without the influence of solar radiation and with different temperature control measures under the same solar radiation intensity is compared and analyzed. In addition, more targeted low-heat pouring block surface insulation measures are proposed and analyzed based on the monitored temperature data and finite element calculation results. This research can provide guidance for the formulation and implementation of reasonable temperature control measures for the surface concrete of Baihetan dam pouring blocks, which is of great significance for improving the quality of concrete. Figure 1 shows the overall technology roadmap.

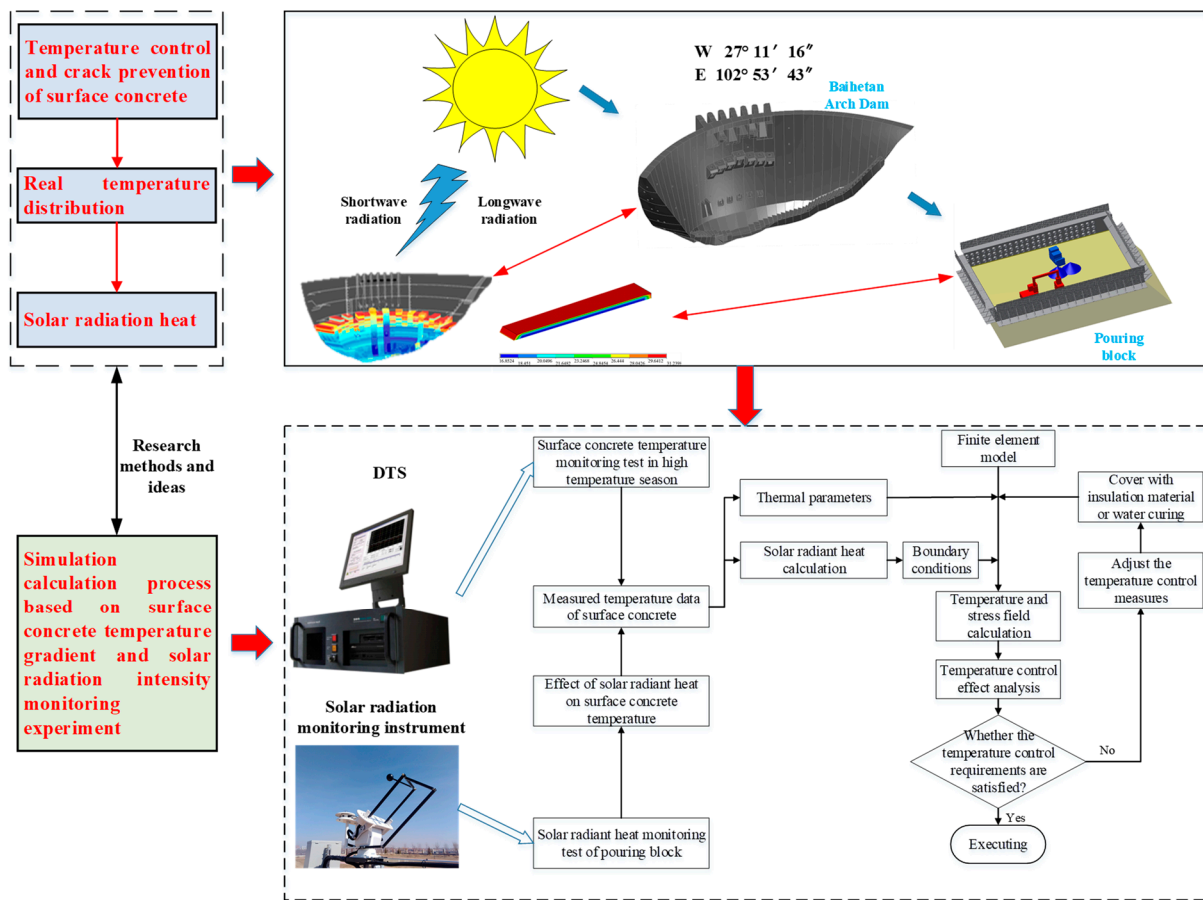


Figure 1. Overall technology roadmap.

## 2. Methodology

### 2.1. Bifilar Embedded Technique of Optical Fiber Based on DTS

To comprehensively monitor the temperature of concrete and acquire more representative and abundant temperature data, it is necessary to adopt a reasonable and reliable embedded optical fiber scheme. In this study, a bifilar embedded technique of optical fiber in the Baihetan arch dam is first put forward. The schematic diagram of the bifilar embedded technique of optical fiber is shown in Figure 2. The bifilar embedded technique refers to the main head of optical fiber being connected to the temperature measuring host by utilizing the tail fiber, and the optical fiber is pulled from the monitoring room to the placement room of optical fiber. The bifilar embedded technique of optical fiber has three advantages. Advantage 1: It can increase the survival rate of embedded optical fiber. Advantage 2: The standby head will be pulled into the monitoring room and connected to the host when the embedded optical fiber is interrupted in pouring blocks by accident. The concrete temperature at the above points of interrupted optical fiber can be monitored continuously. Advantage 3: The monitoring data is obviously symmetrical on the linear structure; the same spatial location has two symmetrical monitoring points, which provides an opportunity and foundation for realizing the precise localization of distributed optical fiber temperature measurement points [36].

The DTS system can linearly monitor the spatial-temporal distribution of concrete temperature in real-time and steadily, which is an automatic monitoring system that is composed of a laser light source, sensor fiber, and monitoring instrument [37]. The fiber is not only a sort of sensing medium but also a kind of transmission medium. The temperature monitoring principle of DTS is shown in Figure 2. When a laser pulse travels through the optical fiber, Raman scattering occurs at every point along the fiber. Since scattering light is isotropic, only partial scattering light returns along the optical fiber. If we set the start

time as the laser pulse going into the optical fiber, the scattering echo signals that the input terminal receives the pulse at time  $t$  and indicates a distance of  $L$  from the scattering point to the input terminal. The laser pulses in the optical fibers have traveled a distance of  $2L$ . The distance  $L$  can be expressed as  $L = ct/2n$ , where  $c$  is the light speed in the vacuum and  $n$  is the refractive index of optical fiber [38–42].

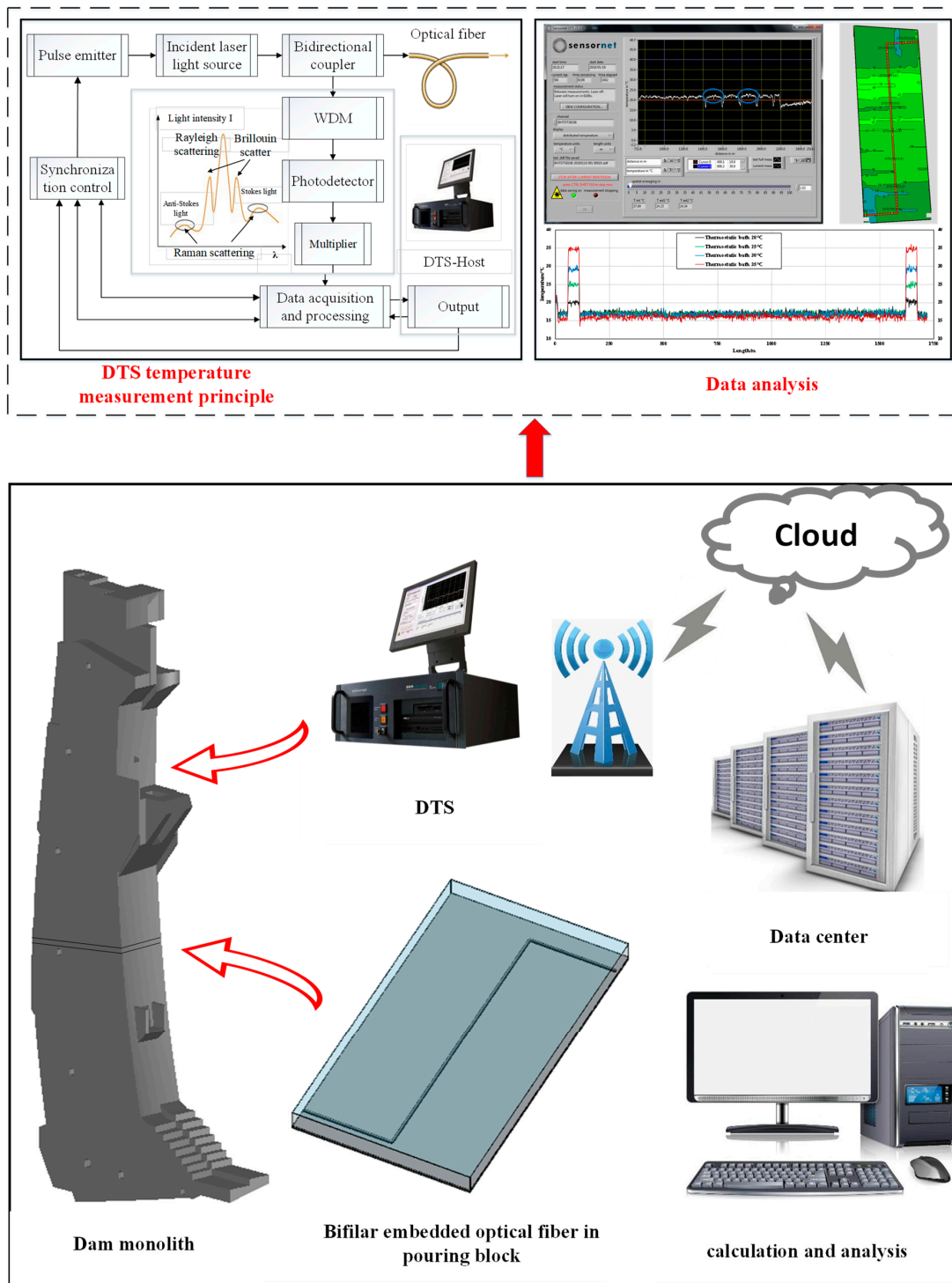


**Figure 2.** Schematic diagram of the bifilar embedded technique of optical fiber based on DTS and the temperature monitoring principle of DTS.

When the light travels through the optical fiber, the incident light's photons are scattered by an inelastic collision with optical photons in the fiber. The scattered light can be sorted into Stokes light and anti-Stokes light. Keeping the external parameters and the optical fiber parameters unchanged, a functional relationship is formed between the temperature  $T$  at the monitoring position and the anti-Stokes light's optical power, which can be written as follows [43]:

$$T = \frac{hcv}{k \left[ \ln \alpha - \ln \left( \frac{I_a}{I_s} \right) \right]} \quad (1)$$

where  $I_a$  is the anti-Stokes light's optical power;  $I_s$  is the Stokes light's optical power;  $\alpha$  is the temperature correlation coefficient;  $h$  is the Planck coefficient (j·s);  $c$  is the light speed in vacuum (m/s);  $v$  is the Raman shift amount ( $\text{m}^{-1}$ );  $k$  is the Boltzmann constant (J/K); and  $T$  is the Kelvin rating (K).

Figure 2 shows a schematic diagram of the bifilar embedded technique of optical fiber based on DTS and the temperature monitoring principle of DTS.

## 2.2. Solar Radiation Loading Model in the Pouring Block

### 2.2.1. Calculation Principle of an Unsteady Temperature Field

According to the theory of heat conduction, the solid, unstable temperature field should satisfy [44]:

$$\frac{\partial T}{\partial t} = a \left( \frac{\partial^2 T}{\partial x^2} + \frac{\partial^2 T}{\partial y^2} + \frac{\partial^2 T}{\partial z^2} \right) + \frac{\partial \theta}{\partial t}, \quad (2)$$

where  $T$  is the concrete temperature,  $t$  is the time,  $a$  is the thermal diffusivity of mass concrete, and  $\theta$  is the adiabatic temperature rise of concrete.

The inside of the concrete block is lined with a cooling water pipe to reduce the temperature of the concrete. When performing a temperature field simulation calculation, the cooling water pipe can be regarded as a negative heat source, and the equivalent heat conduction equation of the cooling water pipe is:

$$\frac{\partial T}{\partial t} = a \frac{\partial^2 T}{\partial x^2} + (T_p - T_w) \frac{\partial \varnothing}{\partial t} + \theta_0 \frac{\partial \varphi}{\partial t}, \quad (3)$$

where  $T_p$  is the initial temperature of the concrete,  $T_w$  is the water temperature,  $\varnothing$  is the water-cooling function, and  $\varphi$  is the temperature rise function.

However, in the actual project, the water-passing cooling scheme is dynamically changed, and the water-passing is not performed with a fixed water flow rate and water temperature  $T'$ . Therefore, when calculating the temperature field, the equivalent heat conduction equation for water pipe cooling under multi-speed water temperature conditions should be adopted [44]:

$$\frac{\partial T'}{\partial t} = a \frac{\partial^2 T'}{\partial x^2} + (T_i - T_{wi}) \frac{\partial \varnothing}{\partial t} + \theta_0 \frac{\partial \varphi}{\partial t}, \quad (4)$$

where  $T_{wi}$  is the water temperature in grade  $i$  and  $T_i$  is the average concrete temperature at the beginning of applying the water temperature in grade  $i$ .

### 2.2.2. Influence of the Principle of Solar Radiation Heat on the Concrete Temperature Field

Considering the surface of a semi-infinite body, as shown in Figure 3, it is assumed that three-point thermometers (A, B, and C) are placed on the concrete block. The solar radiant heat is calculated using a point thermometer. It is assumed that at a certain moment, the measured temperatures of the three-point thermometer are  $T_A$ ,  $T_B$ , and  $T_C$ , the surface temperature of the concrete is  $T_s$ , and the temperature is  $T_{a0}$ . If the coordinate origin is moved to point thermometer A, the temperature at point  $x$  is  $T_s = T(x)$ ; that is, surface temperature  $T_s = T(-a)$ .

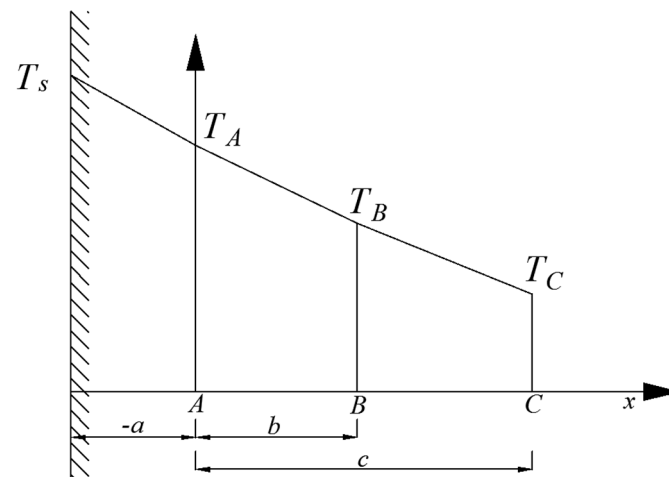


**Figure 3.** Surface temperature distribution of concrete.

The concrete block surface temperature is expressed as follows:

$$T_s = T(x) = k_1 + k_2x + k_3x^2 \quad (5)$$

When  $x = 0$ ,  $T = T_a = k_1$ .

When  $x = b$ ,  $T = T_b = k_1 + k_2b + k_3b^2$ .

When  $x = c$ ,  $T = T_c = k_1 + k_2c + k_3c^2$ .

The following expression is obtained from the above three formulas:

$$k_1 = 0 \quad (6)$$

$$k_2 = \frac{c^2T_b - b^2T_c - (c^2 - b^2)T_a}{bc(c - b)} \quad (7)$$

$$k_3 = \frac{bT_c - cT_b + (c - b)T_a}{bc(c - b)} \quad (8)$$

On the concrete surface  $x = -a$ ; then

$$\begin{cases} T_s = k_1 - k_2a + k_3a^2 \\ \left(\frac{\partial T}{\partial x}\right)_s = k_2 - 2ak_3 \end{cases} \quad (9)$$

where  $\partial T/\partial x$  is the temperature gradient.

Solar radiant heat  $R$  is calculated by the following formula:

$$R = \beta(T_s - T_{a0}) - \lambda \left(\frac{\partial T}{\partial x}\right)_s, \quad (10)$$

where  $\beta$  is the surface heat release coefficient of concrete, and  $\lambda$  is the thermal conductivity of concrete.

In engineering, solar radiant heat is applied to the boundary conditions of concrete in the form of heat flow, but this method is not convenient for concrete temperature field calculation. To this end, Academician Zhu [44] proposed the comparison of solar radiation to the temperature increment  $\Delta T_a$ , and then considered the effect of solar radiant heat on the concrete temperature field by means of equivalent heat transfer boundary conditions. This method has been well validated in many studies [45–47].

$$\Delta T_a = \frac{R}{\beta} \quad (11)$$

### 2.3. Experimental Data Analysis Process

In this study, a DTS system is applied to monitor the surface temperature gradient of concrete in real time, and a solar radiation heat monitoring test is also carried out based on the Baihetan project. Based on this, a solar radiation loading model and a finite element model of a typical pouring block are established. Under the influence of air temperature and solar radiation, the temperature change process of concrete at different depths with time can be obtained in real-time. Combined with the measured temperature data and different calculation conditions, the surface temperature changes of medium and low-heat concrete under solar radiation are analyzed, and the temperature control effect of surface concrete with different surface insulation measures is further analyzed.

## 3. Case Study

### 3.1. Project Overview

The Baihetan Hydropower Station on the Jinsha River is located in the lower reaches of the Jinsha River, bordering Ningnan County, Sichuan Province, and Qiaojia County, Yunnan Province. The geographical location of Baihetan dam, is shown in Figure 4. The dam crest height of Baihetan dam is 834 m, and the maximum dam height is 289 m [40]. The dam area is in the subtropical monsoon region. It is affected by the southwest monsoon all year. The weather is sunny and dry. The valley area is dry and hot, and the sunshine is strong. The annual maximum temperature reaches 42.7 °C. The high-temperature season starts in April and ends in October. Under the conditions of high temperatures and intense solar radiation in summer, solar radiation heat is transmitted to the concrete blocks, which makes the moisture evapotranspiration of the surface concrete faster, the temperature fluctuation larger, and the influence of the diurnal temperature different. A nonlinear temperature difference between the inside and outside of concrete is produced, which has a certain impact on the pouring block's surface thermal insulation and moisturizing work. The early strength of low-heat concrete is low, and in the above environment, the risk of cracking is undoubtedly increased.

### 3.2. Temperature and Solar Radiation Monitoring Test Plan

Distributed fiber has the advantage of real-time online monitoring and the monitoring of a large amount of data. It can be used to continuously monitor the temperature of concrete, and it can reflect the temperature change of the concrete more than a point thermometer, which can only monitor the single point temperature inside the concrete. Therefore, in this research, distributed optical fiber is used to monitor the surface temperature of concrete blocks. Distributed optical fibers are embedded at 10 cm, 20 cm, 40 cm, and 60 cm away from the top of concrete blocks. To ensure that the fiber is parallel to the top surface of a concrete block, the fiber is attached to the special steel frame, and the steel frame is placed perpendicular to the top surface of the concrete block. The top of the frame is 10 cm away from the top surface of the concrete block. At the same time, the solar radiation monitoring test of a typical pouring block is carried out. The temperature and solar radiant monitoring test plans are shown in Figure 5. The layout of the optical fiber of the temperature monitoring test for the concrete temperature gradient on the surface of a concrete block is shown in Figure 5, including the DTS system, the leading optical fiber, the monitoring optical fiber, and the fixed support. Meanwhile, the solar radiation recorder is positioned on the pouring block to monitor the solar radiation intensity of the concrete surface.

### 3.3. Field Test and Results Discussion

According to the test scheme for concrete temperature monitoring and solar radiation monitoring, a field test of distributed optical fiber temperature measurement and solar radiation monitoring of a typical pouring block is carried out. Figure 6 shows the field test diagram for simultaneous distributed optical fiber temperature measurement and solar radiation monitoring in the same pouring block. The distributed optical fiber temperature

measurement test mainly adopts the method of embedding the optical fiber on the fixed bracket for continuous temperature monitoring. Additionally, for solar radiation monitoring, a PC-2B multi-channel solar radiation recorder is used to continuously monitor the solar radiation intensity.

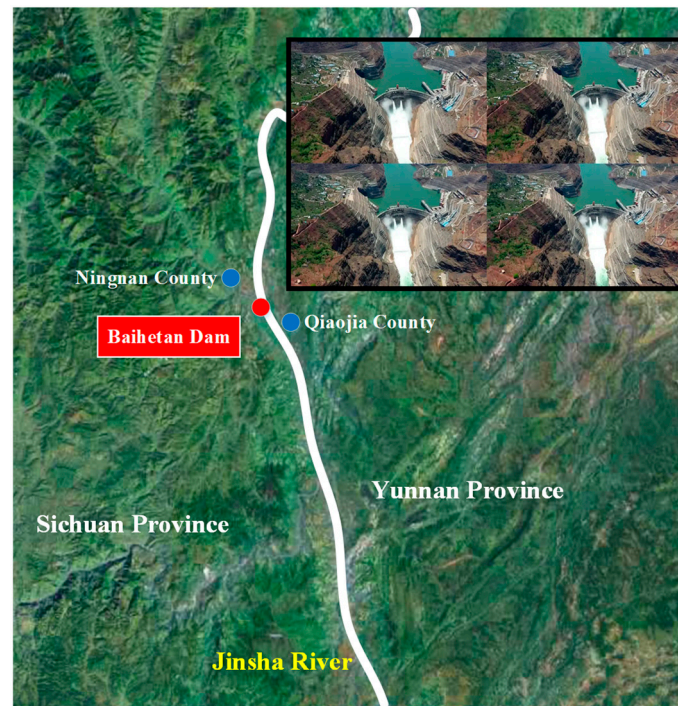


Figure 4. Geographical location map of Baihetan dam.

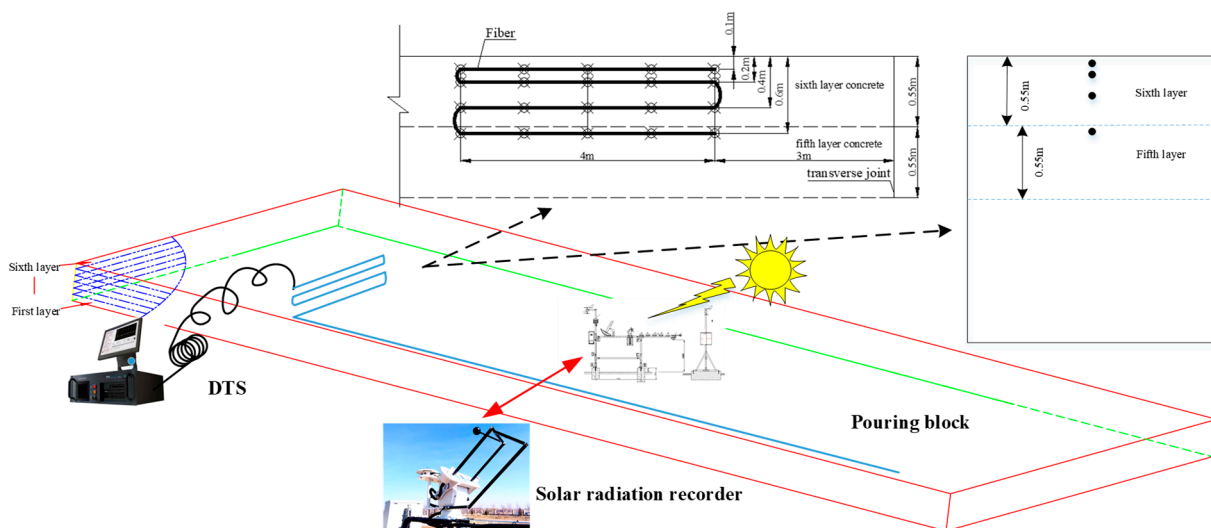


Figure 5. Schematic diagram of the temperature and solar radiant monitoring test plan.

In addition, the tested pouring block is poured on September 24, with an interval of nine days. During the whole interval, the upper and lower surfaces and the transverse surface are insulated with a benzene board, and the top surface is not covered with insulation material. The sunshine is strong for five days before the interval, and the maximum temperature reaches  $32\text{ }^{\circ}\text{C}$ . The surface temperature of the concrete block changes significantly. Therefore, the monitoring data for the first five days of age is selected for display. The temperature measurement curve of the typical measuring point fiber at different depths from the top surface of the pouring block and the monitoring of the solar radiation inten-

sity with the influence of sunshine for five consecutive days are shown in Figure 7. The acquisition frequency of solar radiation heat is half an hour, and the acquisition frequency of DTS temperature measurement data is two hours.



**Figure 6.** Diagram of the temperature and solar radiant monitoring field test.

According to the analysis of the monitoring data, the temperature curve of the concrete within the depth of 0.2 m from the top surface fluctuates greatly within five days, and the maximum daily variation is 12.28 °C. In the first two days of age, the temperature of the concrete 40 cm from the top surface does not change much, but after 2.5 d, the temperature curve fluctuates significantly, mainly due to the external environment and hydration heat. The concrete temperature curve from the top surface of 60 cm has no obvious fluctuation, and the temperature change trend is consistent with the internal concrete temperature change trend. It can be seen that the influence of solar radiant heat on the surface temperature of low-heat concrete is within 40 cm of the top surface, and the solar radiant heat has the most obvious influence on the temperature of concrete within 20 cm of the top surface.

It can be seen from the measured data that the higher the ambient temperature is, the greater the temperature difference is between the concrete 10 cm from the top surface and 60 cm from the top surface. When the external temperature is 32 °C, the temperature difference between the concrete 10 cm and 60 cm away from the top is as high as 8.3 °C. It can be predicted that the temperature difference between the surface concrete and the internal concrete is larger. When the outside temperature fluctuates around 25 °C, the temperature difference between the concrete 10 cm from the top surface and 60 cm from the top surface is within 1 °C.

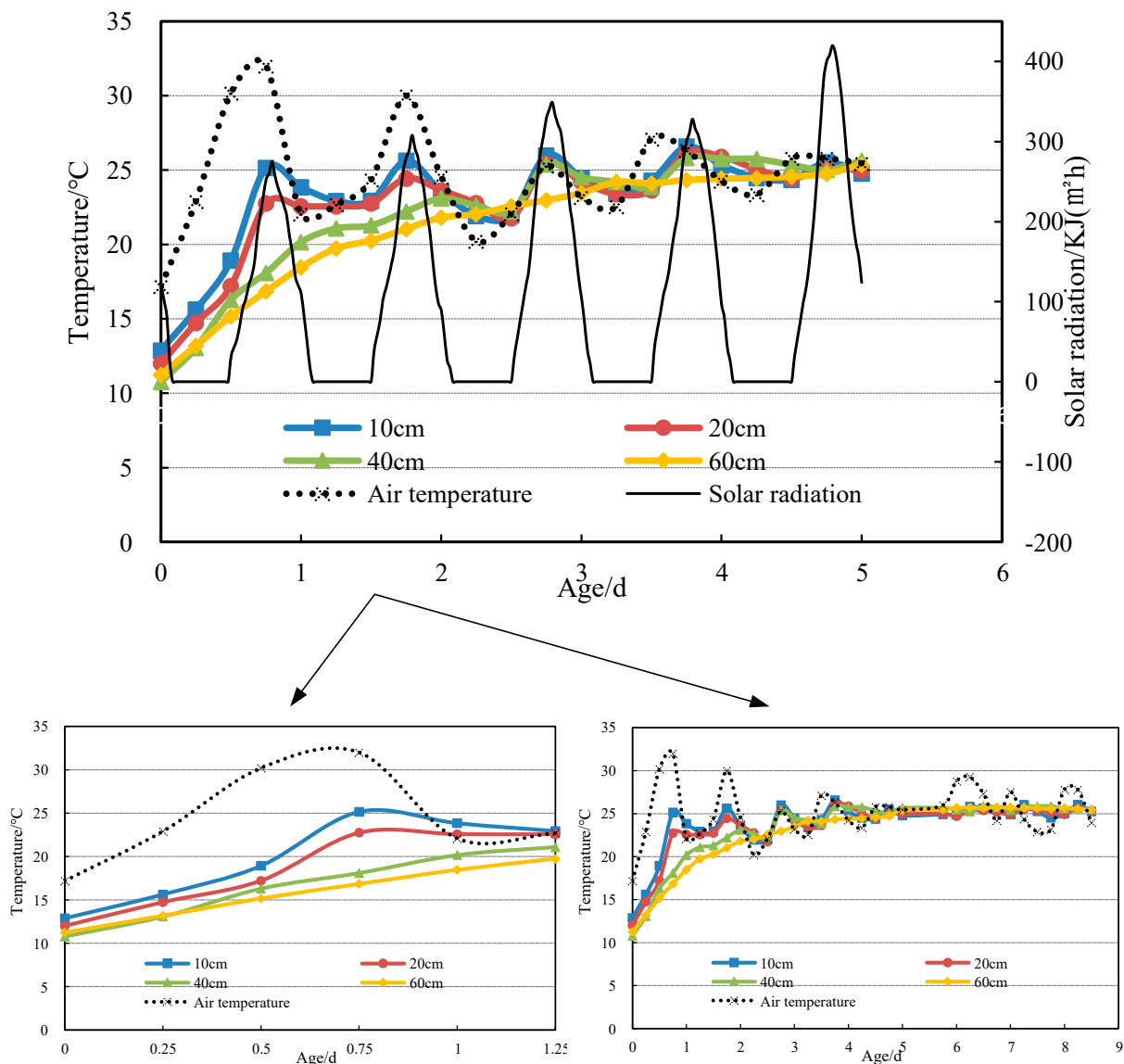


**Figure 7.** The temperature measurement curve of the typical measuring point fiber at different depths from the top surface of the pouring block and the monitoring of the solar radiation intensity.

### 3.4. Calculation Model and Boundary Conditions

To simplify the analysis, two continuous pouring blocks, including test concrete blocks, are selected as the analysis objects, and the finite element calculation model is established. The concrete block uses C<sub>180</sub>40 low-heat concrete with a layer thickness of 3 m, and each concrete block is divided into six layers. The concrete mix ratio is shown in Table 1, and the raw materials of concrete include cement, coal fly ash, aggregate, admixtures, etc. The thermal parameters of concrete are shown in Table 2. The cooling water pipe layout and cooling water parameters are shown in Figure 8. The concrete temperature of pouring blocks can be cooled by embedded cooling water pipes arranged in a quincunx shape. The temperature amplitude caused by hydration heat in concrete can be reduced by cooling water in the pipes to avoid excessive temperature rises in concrete. The hexahedral eight-node parametric element is used to divide the finite element mesh, and the mesh is divided every 0.5 m along the height direction of the concrete block and encrypted 60 cm from the top surface of the test concrete block. The model is divided into a total of 39,312 units and 43,529 nodes, as shown in Figure 9. When calculating, the side, top, and upstream and downstream surfaces of the concrete block are the third type of boundary conditions, and the calculated parameters are all actual values. The actual water temperature, water flow,

and water time are adopted. In the calculation process, the equivalent heat conduction equation of water pipe cooling is used to simulate the cooling effect of cooling water pipe and calculate the temperature field of the pouring block. Meanwhile, the daily average temperature of concrete can be obtained by field testing. The daily average air temperature can be obtained from local weather stations.

The contact heat transfer between the concrete surface and air (fluid) is the third boundary condition. It is assumed that the heat flux entering the concrete surface is proportional to the difference between the concrete surface temperature  $T$  and the air temperature  $T_{a0}$  ( $T = T_{a0}$ ):

$$-\lambda \frac{\partial T}{\partial n} = \beta(T - T_{a0}) \quad (12)$$

where  $-\lambda \frac{\partial T}{\partial n}$  is the heat flux and  $\beta$  is the surface heat release coefficient.

The solar radiation heat is mainly applied to the finite element through the second boundary condition, and the air temperature is applied to the finite element through the third boundary condition. For the convenience of calculation, the solar radiation heat is converted into the third type of boundary conditions by the second type of boundary conditions; that is, the solar radiation heat is equivalent to the air temperature increment. Then form a comprehensive equivalent temperature with the air temperature and apply it to the concrete temperature field boundary.

$$-\lambda \frac{\partial T}{\partial n} = \beta(T - T_{a0}) - R \quad (13)$$

The influence of solar radiation heat on the temperature field of concrete is equivalent to the temperature increment  $\Delta T_{a0}$  of the concrete's external environment.

$$\Delta T_{a0} = \frac{R}{\beta} \quad (14)$$

The comprehensive equivalent temperature  $T_{a0}^*$  of air temperature increment and air temperature can be expressed as follows:

$$T_{a0}^* = \Delta T_{a0} + T_{a0} \quad (15)$$

**Table 1.** Concrete mix ratio information.

Concrete Mix Ratio	Four Gradations	Water-Binder Ratio	Coal Fly Ash (%)	Sand Ratio (%)	Water Consumption (kg/m <sup>3</sup> )	Water Reducing Agent (%)	Air Entraining Agent (%)
		0.42	35	23	85	0.6	0.045

**Table 2.** Thermal parameters of concrete.

Parameter	Value
Density (kg/m <sup>3</sup> )	21.16
Specific heat (kJ/(kg °C))	1.01
Thermal conductivity (kJ/(m h °C))	7.28
Thermal diffusivity (m <sup>2</sup> /h)	0.002834
Thermal radiation absorption rate	0.65

### 3.5. Inversion of Concrete Thermal Parameters

It can be known from Equations (10) and (11) that the solar radiant heat and its equivalent calculation result for the temperature increment are affected by the thermal parameters of the concrete. Therefore, to improve the reliability of the calculation results, it

is first necessary to carry out the inversion of the thermal parameters of low-heat concrete. The inversion of the thermal parameters of low-heat concrete is based on a BP neural network [42,45]. In this research, the adiabatic temperature rise  $\theta$ , the temperature rise law  $n$ , and the surface heat release coefficient  $\beta$  are selected for inversion. The results are shown in Table 3.

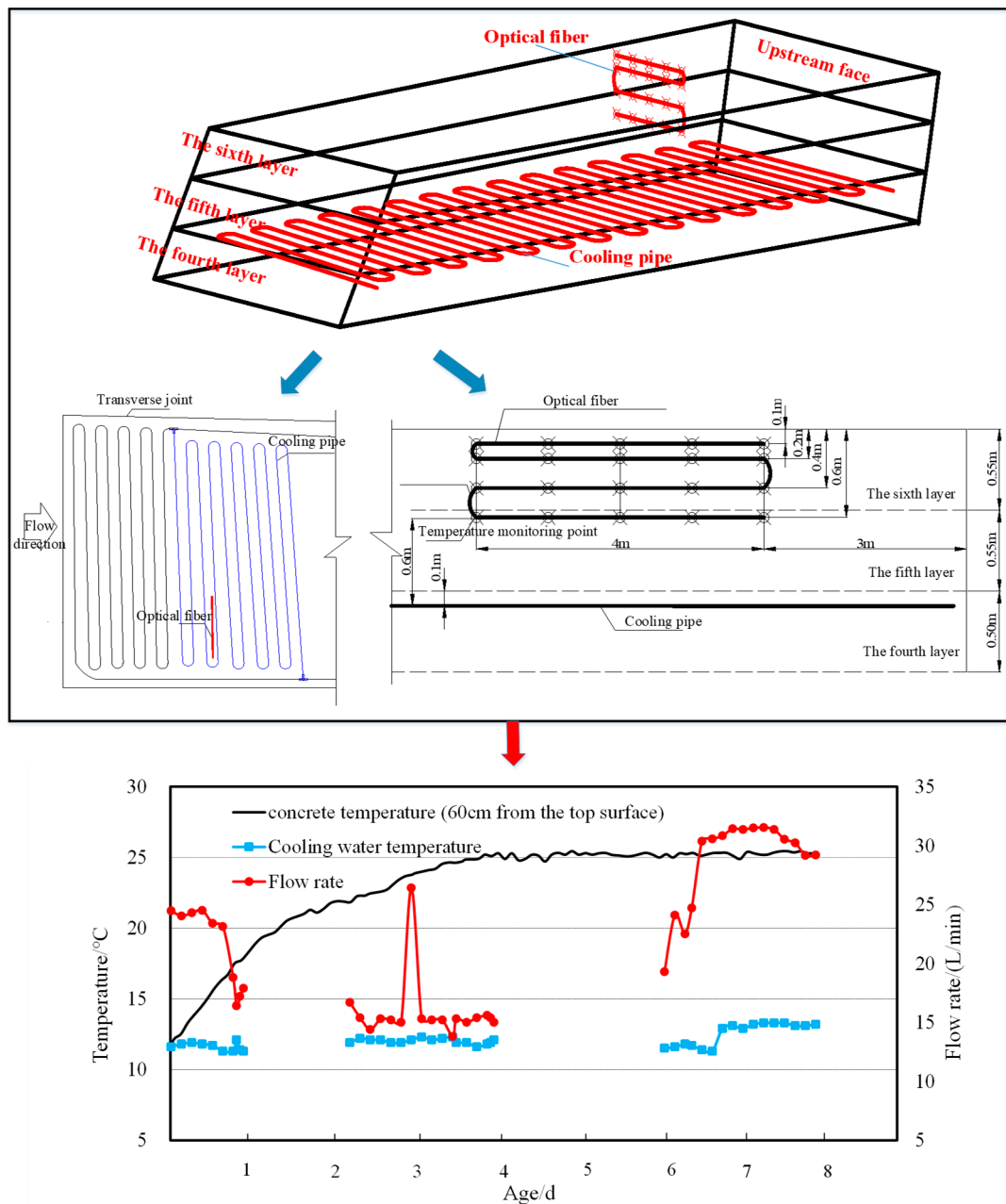


**Figure 8.** Cooling water pipe layout and cooling water parameters.

As shown in Figure 9, the monitoring temperature of the center point for the model in a concrete block is used to compare with the calculated temperature. To verify the accuracy of the inversion value, the inversion results are input into the temperature field simulation program for calculation, and the calculated temperature value is obtained and compared with the measured temperature. The relative error between the measured temperature and the calculated temperature is also calculated. The maximum relative error is only about 4%, which verifies the high accuracy of the inversion value. The comparison curve and the relative errors between the measured and calculated temperatures are shown in Figure 10.

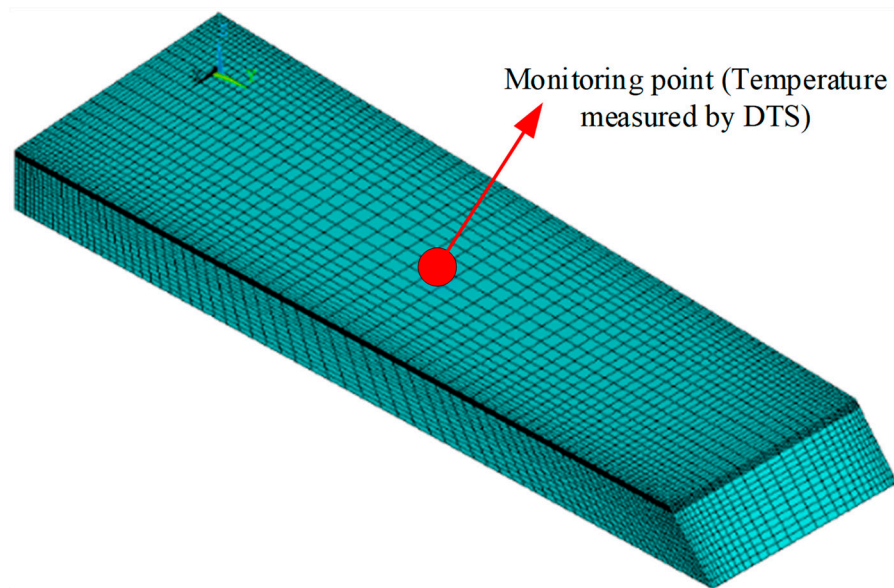


**Figure 9.** Finite element model of a typical concrete block.

**Table 3.** Parameter inversion results.

Parameter	$\theta$ ( $^{\circ}\text{C}$ )	$n$	$\beta$ ( $\text{kJ}/(\text{m}^2 \cdot \text{d} \cdot ^{\circ}\text{C})$ )
Inversion result	21.16	2.86	440.03

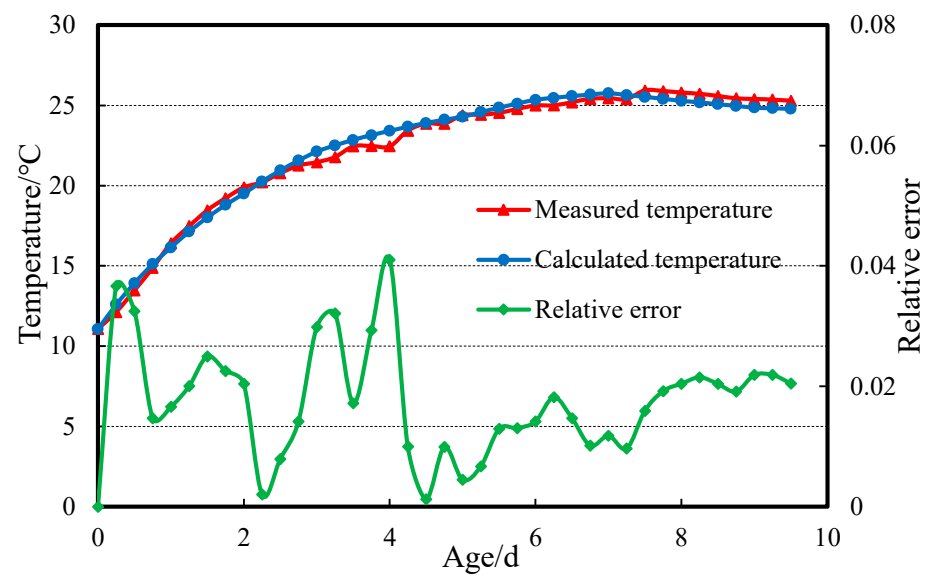


**Figure 10.** Comparison curve and relative errors between measured and calculated temperatures.

As can be seen from Figure 10, the calculated values are consistent with the overall trend of the measured values. The correlation coefficient  $R$  of the curve in the figure is 0.995. It can be seen that the temperature calculated by the parameter inversion value is close to the measured temperature, and the measured curve and the calculated curve have a higher fitting degree. Therefore, the adiabatic temperature rise of the low-heat concrete A is 21.16  $^{\circ}\text{C}$ , the temperature rise law  $n$  is 2.86, and the surface heat release coefficient  $\beta$  is 440.03  $\text{kJ}/(\text{m}^2 \cdot \text{d} \cdot ^{\circ}\text{C})$ .

### 3.6. Results and Discussion

#### 3.6.1. Influence of Solar Radiant Heat on the Temperature Field of Low-Heat Concrete

The temperature data at different depths of the test concrete block surface are obtained with the monitoring scheme shown in Figure 2. Based on this, the surface temperature of the test concrete block and the surface temperature gradient of the concrete are calculated using Equation (9). Finally, the actual value of the absorbed solar radiant heat of concrete is calculated using Equation (10). In the calculation process, the surface heat release coefficient  $\beta$  of the concrete surface adopts the inversion value discussed in Section 3.5, the thermal conductivity of the concrete adopts a known value, and the air temperature is based on field measurements. The calculation results are shown in Table 4.  $T_a$ ,  $T_b$ , and  $T_c$  are the temperatures 10 cm, 20 cm, and 40 cm from the top surface of the concrete block, respectively.  $T_s$  is the surface temperature of the concrete block.  $T_{a0}$  is the air temperature.  $(\partial T/\partial x)_s$  is the temperature gradient of the concrete block.  $R$  is the actual value of the absorbed solar radiant heat of concrete.  $R/\beta$  is the equivalent temperature increase caused by the action of solar radiant heat. The diagonal bar in Table 4 represents the concrete at a moment that is not affected by solar radiant heat (usually at night or in the early morning).

**Table 4.** Solar radiation heat calculation results.

Age (d)	$T_a$ (°C)	$T_b$ (°C)	$T_c$ (°C)	$T_s$ (°C)	$T_{a0}$ (°C)	$(\partial T/\partial x)_s$ (°C·m <sup>-1</sup> )	$R$ (kJ·(m <sup>2</sup> ·h) <sup>-1</sup> )	$R/\beta$ (°C)
0.25	15.62	14.73	13.06	16.56	22.90	−9.54	/	/
0.50	18.93	17.21	16.29	22.67	30.20	−29.80	40.86	2.23
0.75	25.15	22.74	18.09	31.62	32.00	−24.95	87.55	4.77
1.00	23.84	22.58	20.17	22.94	22.07	−13.24	/	/
1.25	22.93	22.57	21.09	23.03	22.69	0.26	/	/
1.50	22.95	22.40	21.29	23.51	24.35	−5.57	22.01	1.20
1.75	25.63	24.44	22.22	28.10	30.30	−12.71	28.22	1.54
2.00	23.54	23.64	23.10	22.28	24.55	9.97	/	/
2.25	21.93	22.77	22.63	20.48	20.23	10.71	/	/
2.50	21.96	21.76	22.22	21.65	22.08	−6.31	49.24	2.69
2.75	25.99	25.43	25.39	27.67	25.30	−11.00	103.64	5.65
3.00	24.47	24.21	24.53	25.01	23.19	−6.80	/	/
3.25	23.43	23.38	24.22	23.79	22.55	−5.11	/	/
3.50	24.30	23.63	23.87	25.02	27.11	−14.60	68.64	3.74
3.75	26.59	26.10	25.83	27.32	26.32	−8.45	75.09	4.10
4.00	25.32	25.90	25.76	24.40	24.26	−0.81	/	/

To study the influence of solar radiant heat on the temperature field of low-heat concrete, the first five days of the most intense sunshine are taken as a research cycle. Not considering the solar radiant heat effects and considering the solar radiant heat effects are basic conditions 1 and 2. Based on condition 2, the top surface of the concrete block is covered with three different thicknesses of polyethylene coils as the comparative conditions for the analysis of the surface temperature state of the low-heat concrete with different temperature control measures considering the influence of solar radiation heat (conditions 3–5). The conditions are shown in Table 5. The equivalent surface heat release coefficient of different insulation materials is shown in Table 6. The concrete thermal parameters in the temperature field simulation calculation use the inversion values discussed in Section 3.5. When considering the influence of solar radiant heat, the solar radiant heat calculations shown in Table 3 are equivalent to the ambient temperature increment applied to the model

boundary conditions. The calculated time step is 0.25 d. The finite element model is shown in Figure 9.

**Table 5.** Calculation conditions.

Condition	Solar Radiant	Insulation Coverage			
		Upstream Surface	Downstream Surface	Horizontal Joint	Top Surface
1 (Actual condition)	×	/	/	/	/
2 (Basic condition)	✓	/	/	/	/
3	✓	5-centimeter-thick benzene board	3-centimeter-thick benzene board	5-centimeter-thick benzene board	2-centimeter-thick polyethylene coil
4	✓	5-centimeter-thick benzene board	3-centimeter-thick benzene board	5-centimeter-thick benzene board	4-centimeter-thick polyethylene coil
5	✓	5-centimeter-thick benzene board	3-centimeter-thick benzene board	5-centimeter-thick benzene board	5-centimeter-thick polyethylene coil

**Table 6.** Equivalent surface heat release coefficient of different thermal insulation materials.

Materials	3-Centimeter-Thick Benzene Board	5-Centimeter-Thick Benzene Board	2-Centimeter-Thick Polyethylene Coil	4-Centimeter-Thick Polyethylene Coil	5-Centimeter-Thick Polyethylene Coil
Surface Exothermic Coefficient	335.42	216.37	412.46	231.05	189.40

The calculation results demonstrate that:

(1) The comparison curves between the calculated temperature and the measured temperature of concrete at different depths from the top surface under conditions 1 and 2 are shown in Figure 11. Under condition 1, the calculated temperature of the low-heat concrete at different depths from the top of the casting silo is lower than the measured value. The temperature difference between the calculated value and the measured value is obvious 10–20 cm from the top surface. The maximum temperature difference reaches 4.47 °C, and the maximum temperature difference is within 2.4 °C. The general trend of the temperature curve between the calculated value and the measured value 40 cm away from the top surface is similar in the first 2.5 days. The temperature difference is less than 1 °C. In the following days, the difference between the simulated value and the measured value at very few time points is larger; the maximum difference is 2 °C. The difference between the calculated value and the measured value 60 cm away from the top surface is within 1 °C, and the temperature curve of the calculated value and the measured value tends to be consistent as a whole.

(2) Under condition 2, the solar radiation heat is equivalent to the increment of temperature necessary to impose boundary conditions on the calculation model. The results show that the difference between the calculated and measured values at a distance of 10–60 cm from the top surface is less than 1 °C, and the difference between the calculated and measured maximum temperatures is less than 0.7 °C. This shows that the general rule of temperature feedback is better when the solar radiation heat is equivalent to the increment of temperature applied to the boundary conditions of the model, and the simulation results considering the influence of solar radiation heat have high accuracy.

(3) The temperature variation curve of the low-heat concrete at different depths from the top of the casting silo is shown in Figure 12. For the field measured and calculated conditions 3–5, taking the concrete temperature state 10 cm away from the top of the pouring block as an example, when the daytime sunshine is intense, the temperature is above 30 °C and the age is 1–2 days. Compared with the field test conditions and

working condition 3, it can be seen that when the top is covered with a 2-centimeter-thick polyethylene coil, the two concrete temperature peaks 10 cm away from the top are reduced from 25.2 °C and 25.6 °C to 23.8 °C and 25 °C, with decreases of 1.4 °C and 0.6 °C. Due to the possible high temperature and intense sunshine environment, the thermal insulation condition of working condition 3 may not be enough to resist the influence of strong solar radiation heat.

(4) By comparing the field-measured working conditions with working conditions 4 and 5, it can be seen that the temperature control effect of working conditions 4 and 5 is roughly the same. When the top surface of the silo is covered with 4- and 5-centimeter-thick polyethylene coils, the temperature drops of the two types of concrete at a distance of 10 cm from the top surface are 4.1 °C and 1.8 °C and 4.5 °C and 2.3 °C, which effectively control the surface concrete temperature. When the daytime temperature is about 25 °C and the age is 3–5 days, the thermal insulation effects of working conditions 3–5 on the surface concrete of the low-heat concrete are approximately the same, which can effectively control the temperature difference between the inside and outside of the concrete of the casting pouring block and reduce the temperature gradient of the surface concrete.

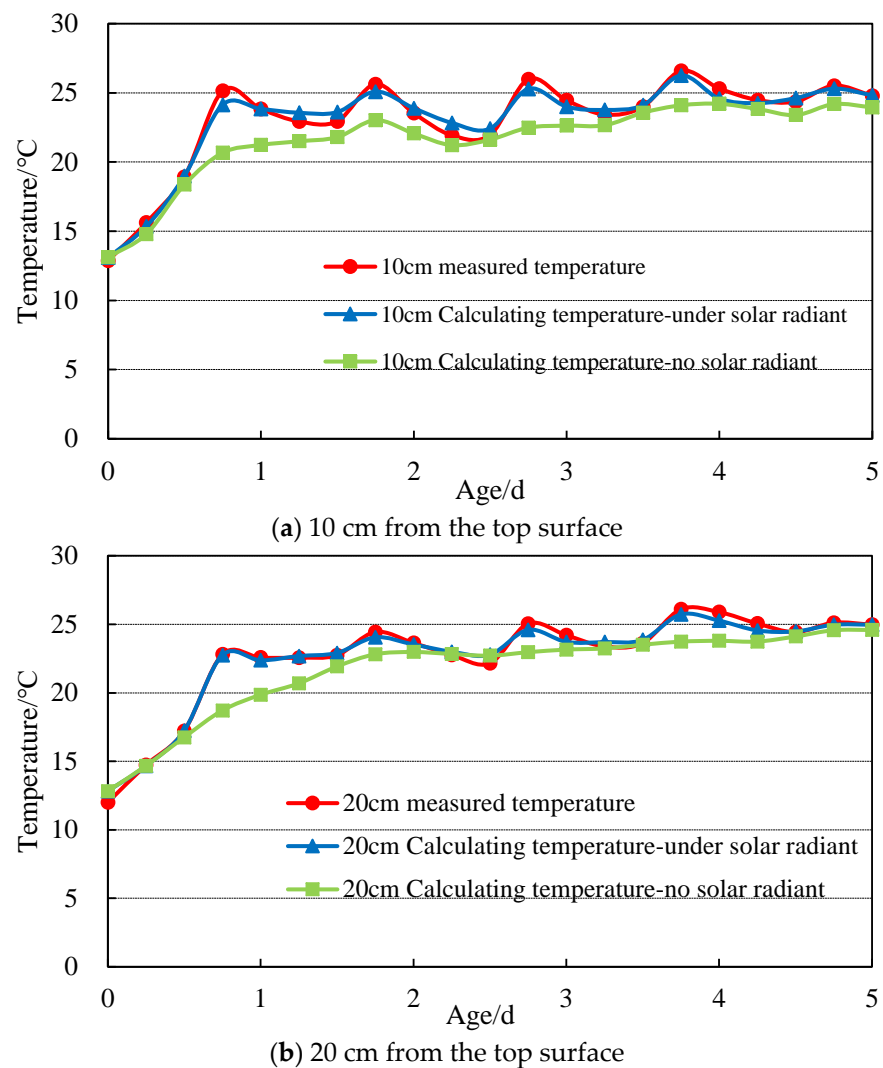
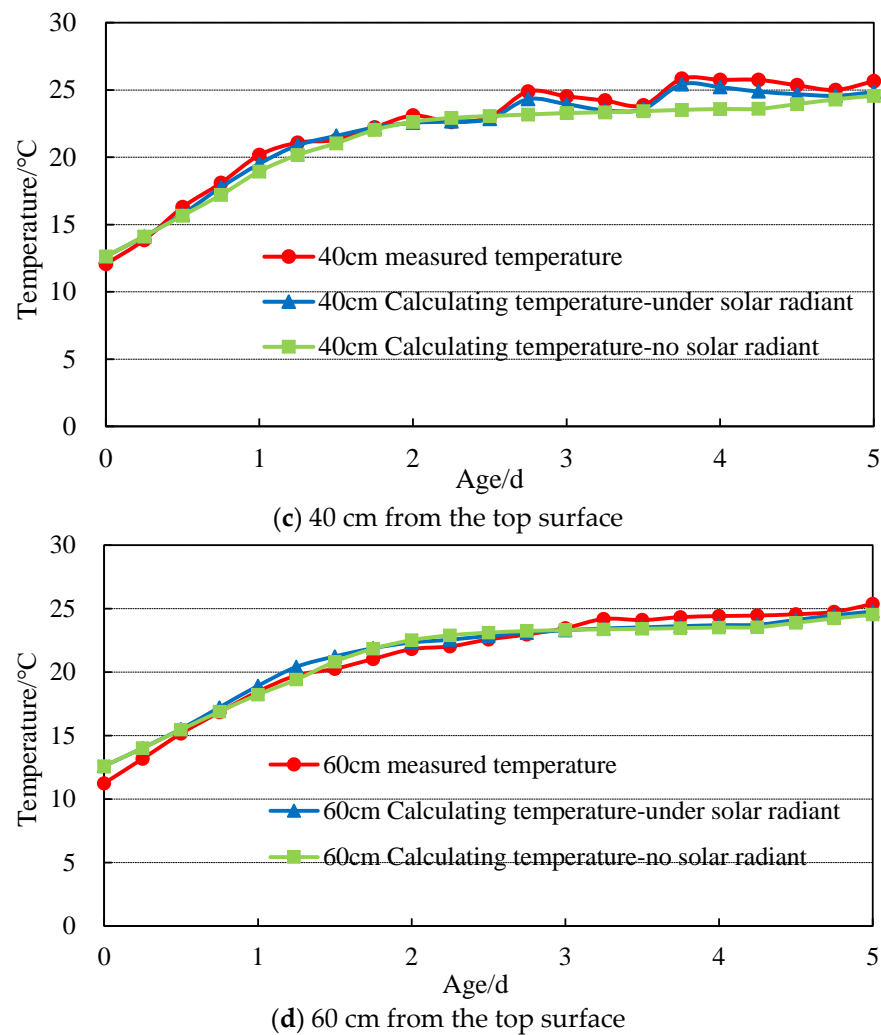


Figure 11. Cont.



**Figure 11.** Comparison between calculated and measured temperatures at different depths from the surface (condition 1 and condition 2).

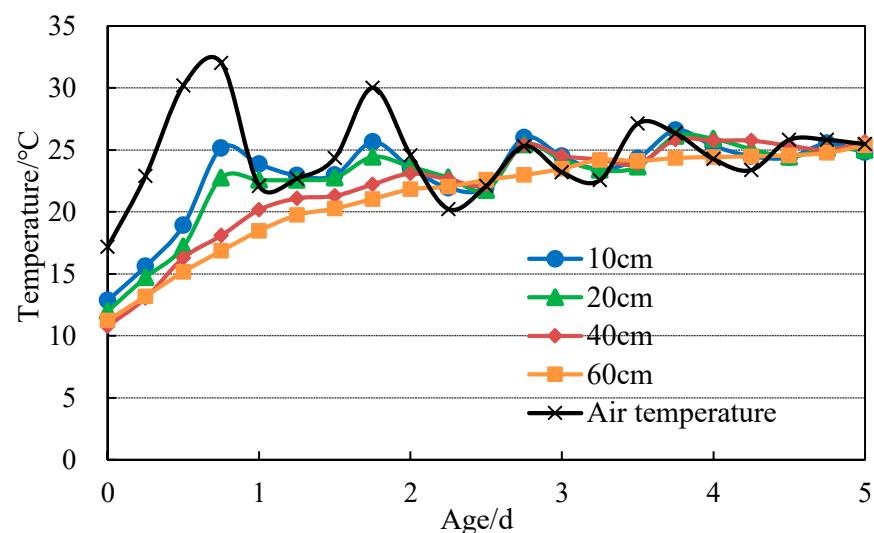
(5) Table 7 shows the maximum temperature gradient of the concrete surface when the top of the casting silo is covered with different-thickness polyethylene coils. When there is no polyethylene coil covering the top surface of the casting silo, the temperature gradient reaches  $16.6\text{ }^{\circ}\text{C}\cdot\text{m}^{-1}$ . Figure 12 shows that when the top of the silo is covered with a 5-centimeter-thick polyethylene sheet, the temperature difference between the concrete 10 cm away from the top and 60 cm away from the top decreases from  $8.3\text{ }^{\circ}\text{C}$  to  $3.6\text{ }^{\circ}\text{C}$ , and the temperature gradient is  $7.2\text{ }^{\circ}\text{C}\cdot\text{m}^{-1}$ , which effectively reduces the maximum temperature gradient of the concrete surface.

(6) Table 8 shows the maximum daily variation of the temperature of the low-heat concrete at different depths from the top under different working conditions. The selected time is the first day after the completion of the pouring. It can be seen from the table that the maximum daily variations of the temperature 10 cm from the top surface under different working conditions are  $12.28\text{ }^{\circ}\text{C}$ ,  $10.73\text{ }^{\circ}\text{C}$ ,  $8.61\text{ }^{\circ}\text{C}$ , and  $8.05\text{ }^{\circ}\text{C}$ . Additionally, the maximum daily temperature changes of the concrete 60 cm from the top surface under different working conditions are  $5.6\text{ }^{\circ}\text{C}$ ,  $4.58\text{ }^{\circ}\text{C}$ ,  $4.22\text{ }^{\circ}\text{C}$ , and  $4.12\text{ }^{\circ}\text{C}$ . This shows that solar radiation heat has a great influence on the temperature of concrete 10 cm from the top surface. Referring to Figure 12, the temperature state of the concrete at a distance of 10 cm from the top surface is taken as an example. When the top surface is not covered with a polyethylene coil, the daytime temperature is above  $30\text{ }^{\circ}\text{C}$ , and the maximum temperature of the concrete at a distance of 10 cm from the top surface is  $1.04\text{ }^{\circ}\text{C}/\text{h}$ . When the top

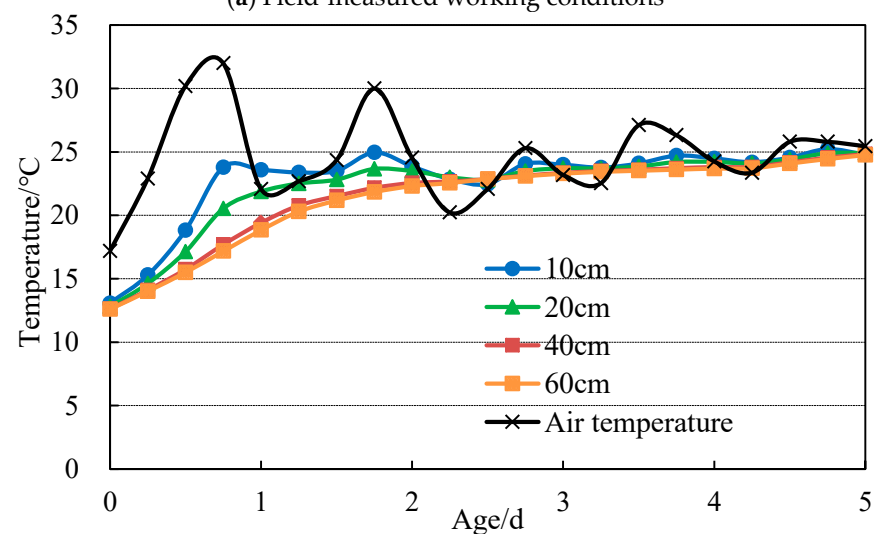
surface is covered with a 5-centimeter-thick polyethylene coil, the maximum temperature change rate of the concrete at a distance of 10 cm from the top surface is reduced from 1.04 °C/h to 0.54 °C/h. Furthermore, the maximum daily variation of the temperature is reduced by 4.23 °C, indicating that covering the top surface with a polyethylene coil is more effective in controlling the maximum daily variation and the variation of the surface concrete temperature rate.

### 3.6.2. Comparison of the Influence of Solar Radiation Heat on the Temperature Field of Medium-Heat Concrete and Low-Heat Concrete

To analyze the difference of solar radiant heat on the temperature state of medium-heat and low-heat concrete, this research is based on the practical experience accumulated by the author's team in the construction of the Xiluodu medium-heat concrete dam project to improve the on-site measured maximum temperature of 5 °C. The effect of solar radiant heat on medium-heat and low-heat concrete is simulated. The consideration and non-consideration of solar radiant heat are set as comparative working conditions, and the differences in the temperature states of the medium-heat and low-heat concrete under the same sunshine conditions are analyzed. The working conditions are shown in Table 9. The thermal parameters of the medium-heat concrete are shown in Table 10. The calculation model is shown in Figure 8.

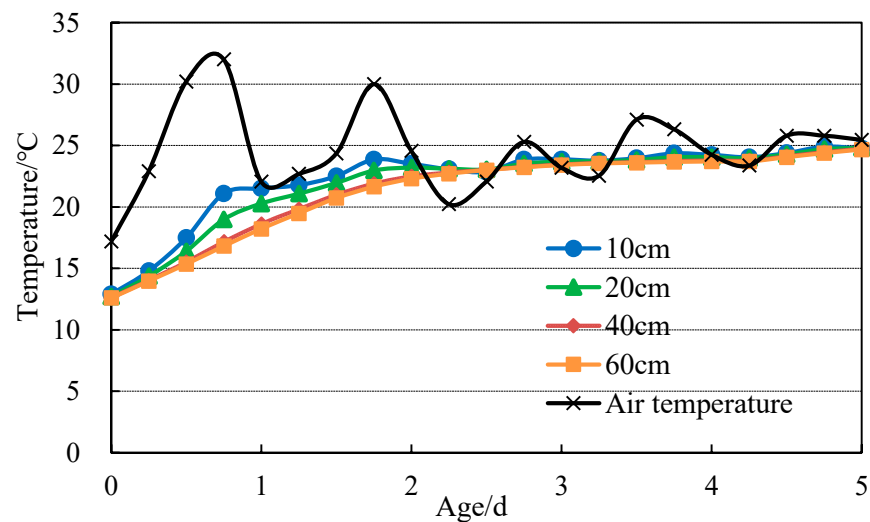


(a) Field-measured working conditions

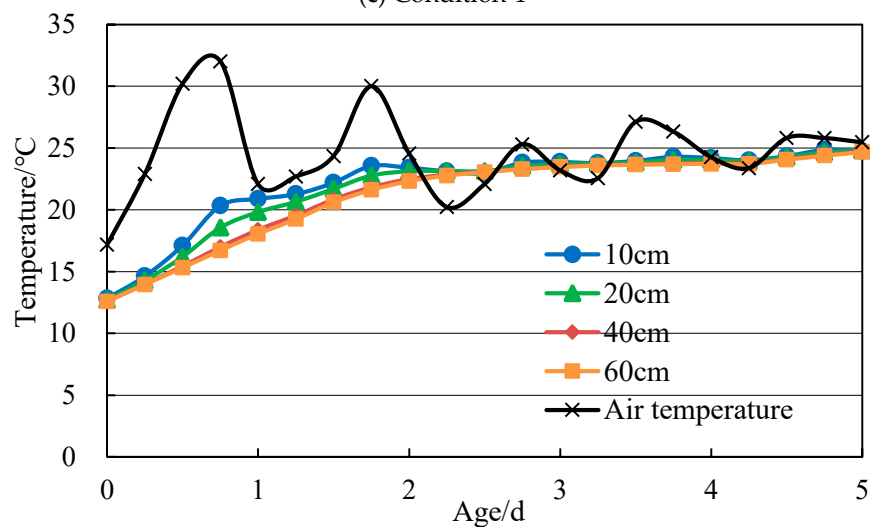


(b) Condition 3

Figure 12. Cont.



(c) Condition 4



(d) Condition 5

**Figure 12.** The temperature process curves at different depths from the surface under different working conditions.

**Table 7.** Maximum concrete temperature gradients for different working conditions.

Condition	Actual	Condition 3	Condition 4	Condition 5
Temperature gradient ( $^{\circ}\text{C}\cdot\text{m}^{-1}$ )	16.6	13.2	8.6	7.2

**Table 8.** Maximum daily variation of temperature at different depths from the surface under different conditions.

Depth	Actual	Condition 3	Condition 4	Condition 5
10 cm	12.28 $^{\circ}\text{C}$	10.72 $^{\circ}\text{C}$	8.61 $^{\circ}\text{C}$	8.05 $^{\circ}\text{C}$
20 cm	10.75 $^{\circ}\text{C}$	7.73 $^{\circ}\text{C}$	6.27 $^{\circ}\text{C}$	5.86 $^{\circ}\text{C}$
40 cm	7.02 $^{\circ}\text{C}$	5.07 $^{\circ}\text{C}$	4.55 $^{\circ}\text{C}$	4.40 $^{\circ}\text{C}$
60 cm	5.6 $^{\circ}\text{C}$	4.58 $^{\circ}\text{C}$	4.22 $^{\circ}\text{C}$	4.12 $^{\circ}\text{C}$

Figure 13 shows the temperature diachronic curves of the medium-heat and low-heat concrete at different depths from the top surface under different working conditions. The calculated results prove that:

**Table 9.** Medium-heat and low-heat concrete calculation conditions table. (× represents no, √ represents yes).

Condition	Types of Concrete	Solar Radiant	Thermal Insulation Material
6	Low-heat concrete	×	×
7	Medium-heat concrete	×	×
8	Low-heat concrete	√	×
9	Medium-heat concrete	√	×

**Table 10.** Thermal parameters of medium-heat concrete.

Thermal Parameters	$\theta$ (°C)	$n$	$\beta$ (kJ/(m <sup>2</sup> ·d·°C))
Medium-heat concrete	25	2.13	1039.2

(1) Without considering the solar radiation heat effect, the calculated temperature of medium-heat concrete within 60 cm of the top surface in the first three days of age is higher than that of low-heat concrete, and the average temperature difference at the same measuring point is less than 2 °C. However, with the increase in age, the temperature change trend of the medium-heat and low-heat concrete is the same.

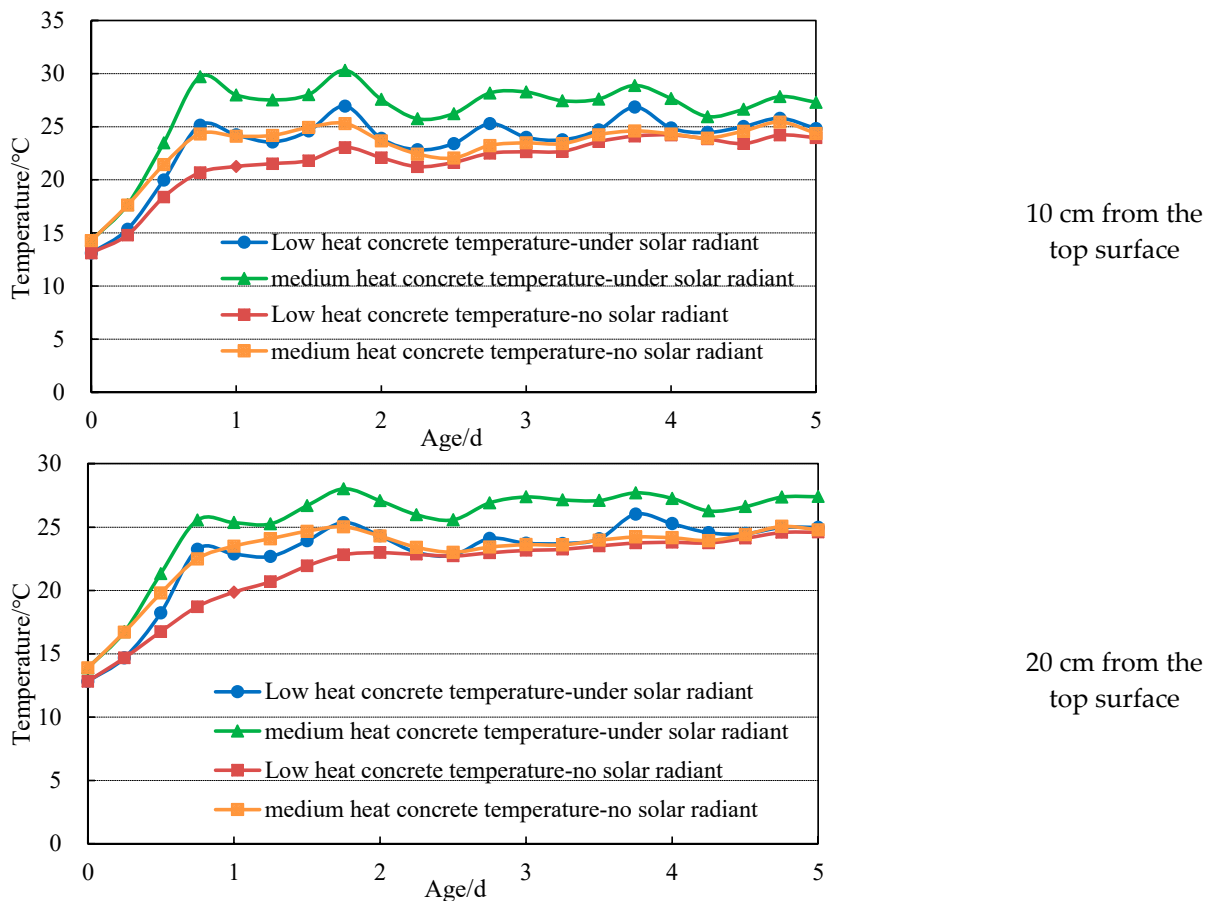


**Figure 13.** Cont.

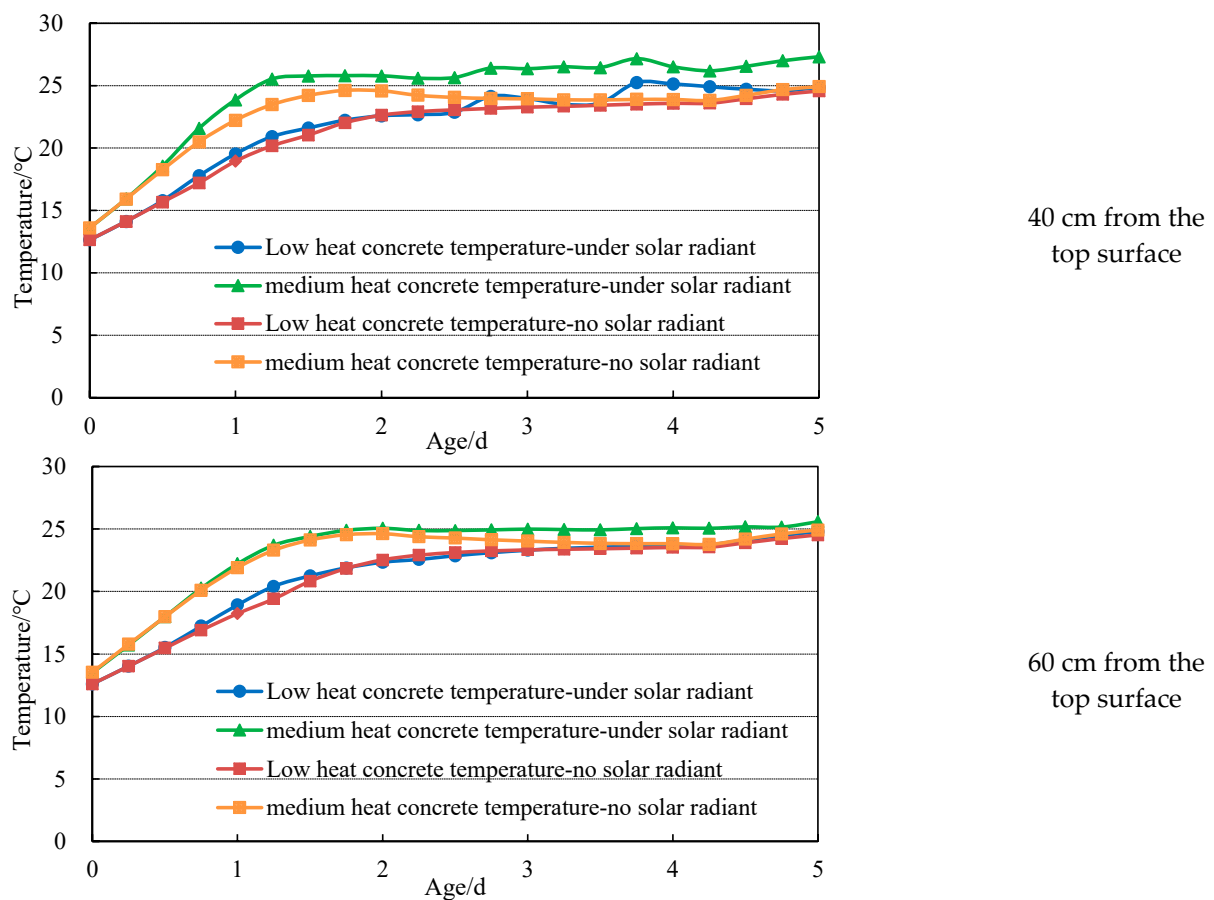


**Figure 13.** Comparison of temperature duration curves between medium-heat concrete and low-heat concrete at different depths of the top surface.

(2) The calculated temperature of the medium-heat concrete 10–60 cm away from the top surface is higher than that of low-heat concrete when considering the solar radiation heat effect. With the action of solar radiation heat, the average difference in the calculated temperature between the medium-heat and low-heat concrete within 40 cm of the top surface is about 3 °C, and the difference between the calculated temperature 60 cm from the top surface is about 2 °C. Then the temperature of medium-heat and low-heat concrete 10 cm away from the top surface is taken as an example. With the action of solar radiation heat, the maximum temperature of the medium-heat concrete reaches 30.3 °C, and the maximum daily variation of temperature reaches 15.4 °C, while the maximum temperature of the low-heat concrete reaches 26.9 °C. The maximum daily variation in temperature reaches 12 °C, and the maximum temperature difference is 3.6 °C.

(3) From Figure 13, it can be seen that with sunshine, the influence depth of solar radiation heat on the surface temperature of medium-heat concrete is less than 40 cm, which is consistent with the influence depth of solar radiation heat on the temperature of low-heat concrete, but the temperature variation of medium-heat concrete is more obvious than that of low-heat concrete in the same period. The maximum temperature gradient of medium-heat concrete is as high as 18.9 °C·m<sup>-1</sup>, and that of low-heat concrete is 15.8 °C·m<sup>-1</sup>. However, in the absence of solar radiation, the maximum temperature gradient of medium-heat concrete is 8.5 °C·m<sup>-1</sup> and that of low-heat concrete is 7.6 °C·m<sup>-1</sup>.

### 3.7. Analysis of Surface Insulation Measures of Pouring Block Considering Solar Radiation Heat

#### 3.7.1. Analysis of the Temperature Control Effect of Surface Concrete Covered with Different Thermal Insulation Materials

Polyethylene coils with thicknesses of 2 cm, 4 cm, and 5 cm are mainly used as the top surface insulation material on the Baihetan site. The actual situation of the construction site is the basic condition for the calculation condition, and the top surface of the pouring block is covered with 2-, 4-, and 5-centimeter-thick polyethylene coils in comparison conditions 1, 2, and 3 for the calculation condition. Table 11 displays the calculation condition information. The concrete-air equivalent surface heat release coefficient for different insulation material coverings is shown in Table 6. Taking the moment when the surface concrete is most affected by solar radiation as the simulation calculation moment, the finite element simulation model of a typical pouring block is established. Figure 14 shows the temperature distribution cloud map of the pouring block along the river center under the basic conditions and comparison conditions 1–3.

**Table 11.** Calculation condition information table.

Calculation Condition	Solar Radiation	Coverage of Thermal Insulation Materials			
		Upstream Surface	Downstream Surface	Horizontal Joint	Top Surface
Basic condition	Yes	/	/	/	/
Comparison condition 1	Yes	5-centimeter-thick benzene board	3-centimeter-thick benzene board	5-centimeter-thick benzene board	2-centimeter-thick polyethylene coil
Comparison condition 2	Yes	5-centimeter-thick benzene board	3-centimeter-thick benzene board	5-centimeter-thick benzene board	4-centimeter-thick polyethylene coil
Comparison condition 3	Yes	5-centimeter-thick benzene board	3-centimeter-thick benzene board	5-centimeter-thick benzene board	5-centimeter-thick polyethylene coil

From Figure 14, it can be seen that with the action of solar radiation heat, the highest temperature of concrete in the test pouring block occurs on the top surface, and the lowest temperature occurs inside the block. The influence of solar radiation heat on the temperature state of the concrete decreases with an increase in depth. Under the basic conditions, the maximum temperature of the top surface is 31.2 °C, and the minimum temperature is 16.9 °C. When the top surface is covered with 2 cm, 4 cm, and 5 cm-thick polyethylene coils, the temperature of the concrete on the top surface decreases to varying degrees. The maximum temperatures under comparison conditions 1, 2, and 3 are 28.6 °C, 25.5 °C, and 24.9 °C, respectively, and the minimum temperature is 16.9 °C.

It can be seen from the cloud map that the highest temperature is mainly concentrated at the boundary in comparison to conditions 2 and 3. Therefore, it is necessary to control the temperature of the boundary concrete in the pouring block during the construction process. The temperature of the top surface is basically maintained at 23.0 °C, which is 7.7 °C lower than the highest temperature under the basic condition. This shows that the shading and heat preservation effects of 4- and 5-centimeter-thick polyethylene coils are better and that these effects effectively reduce the temperature difference between the inside and outside of the concrete.

Furthermore, the concrete temperatures at 10 cm, 20 cm, 40 cm, and 60 cm from the top surface of the pouring block under the basic conditions and the comparison conditions are compared and analyzed to verify the thermal insulation effects of polyethylene coils with different thicknesses on the concrete top surface. Figure 15 displays the temperature duration curves of the concrete at different depths from the top surface of the pouring block under the basic conditions and comparison conditions 1–3. The maximum daily variations of the concrete temperature at different depths from the top surface under the basic conditions and comparison conditions 1–3 are shown in Table 12. Figure 16

displays the duration curves of the temperature change rate of concrete for the basic foundation and comparison conditions 1–3. From the results above, it can be seen that when the temperature is affected by the solar radiation heat, the insulation effect of the top surface covered with 4- and 5-centimeter-thick polyethylene coils is better than that for the 2-centimeter polyethylene coil, which effectively controls the concrete temperature difference within 60 cm from the top surface and reduces the influence of solar radiation heat on the temperature rise of the surface concrete.

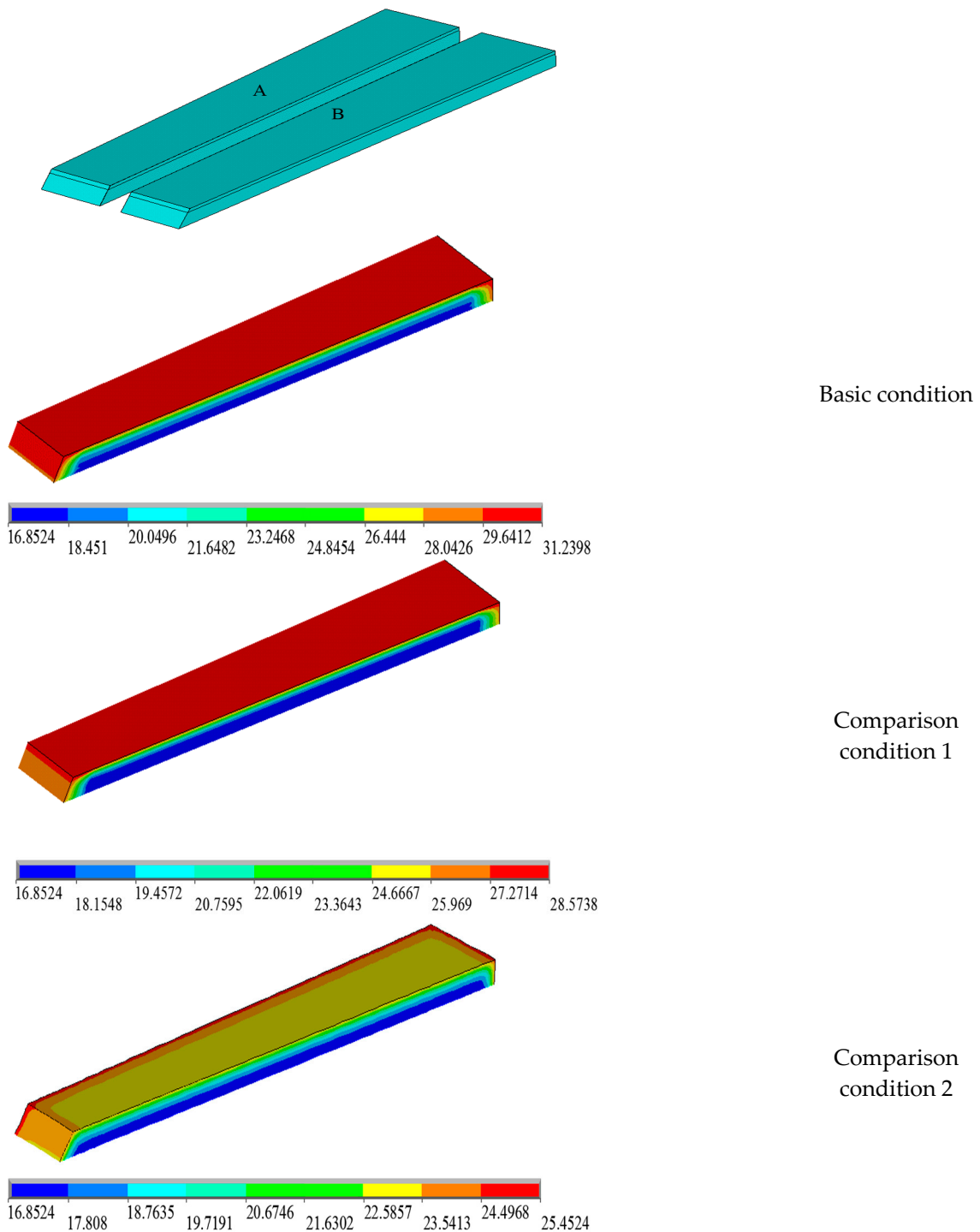
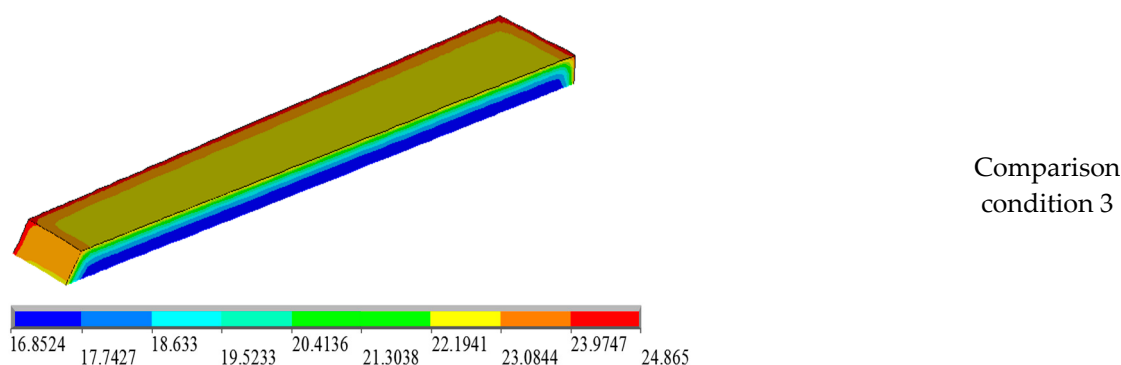


Figure 14. Cont.



**Figure 14.** Temperature distribution cloud map of pouring blocks along the river center under the basic conditions and comparison conditions 1–3 (A and B are the same two parts of the calculation model divided into two parts).

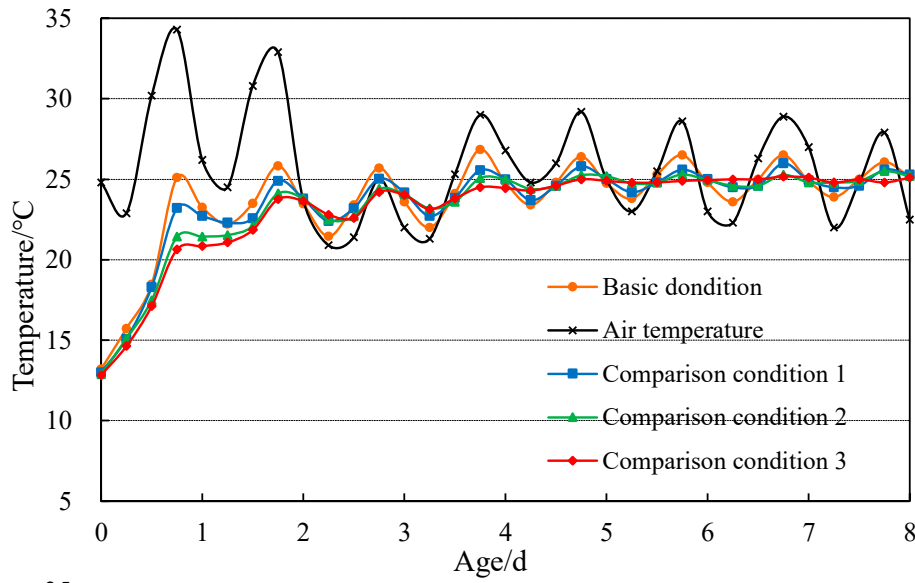
### 3.7.2. Analysis of the Temperature Control Effect of Surface Concrete with Different Types of Water Temperature Flow Maintenance

With the action of strong solar radiation in the high-temperature season, river water is usually extracted to maintain the surface of a new pouring block for a long time to reduce the surface temperature of concrete and control the temperature difference and temperature gradient inside and outside the concrete. The data show that the surface water temperature of the Jinsha River is about 18–22 °C from March to October in the high-temperature season. Based on this, four water temperature flow maintenance conditions are set as the comparison conditions, and the flow maintenance time is in the daytime high-temperature period. At night, the top surface of the pouring block is covered with the 4-centimeter-thick polyethylene coil, as shown in Table 13, for different water temperature flow maintenance calculation tables. Taking the moment when the surface concrete is the most affected by solar radiation as the simulation calculation moment, a finite element simulation model of a typical pouring block is established. The temperature distribution cloud map of the pouring block along the river center under the basic conditions and comparison conditions 4–7 is shown in Figure 17.

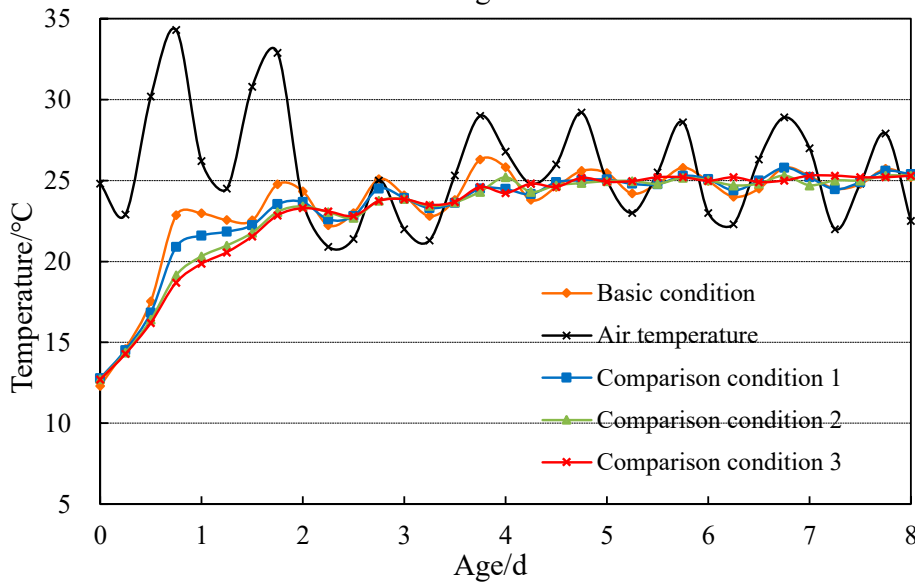
From Figure 17, it can be seen that the temperature of surface concrete can be effectively controlled during the strongest period of solar radiation under comparison conditions 4–7. Compared with the basic condition, the temperatures of the surface concrete can be reduced by 10.7 °C, 10.4 °C, 10.0 °C, and 9.7 °C, and the temperature control effect of the surface concrete is significant.

The temperature state of the surface concrete of the pouring block for different water temperatures is further analyzed, and the simulated temperature and the measured temperature of the concrete at 10 cm, 20 cm, 40 cm, and 60 cm from the top surface of the pouring block are compared and analyzed.

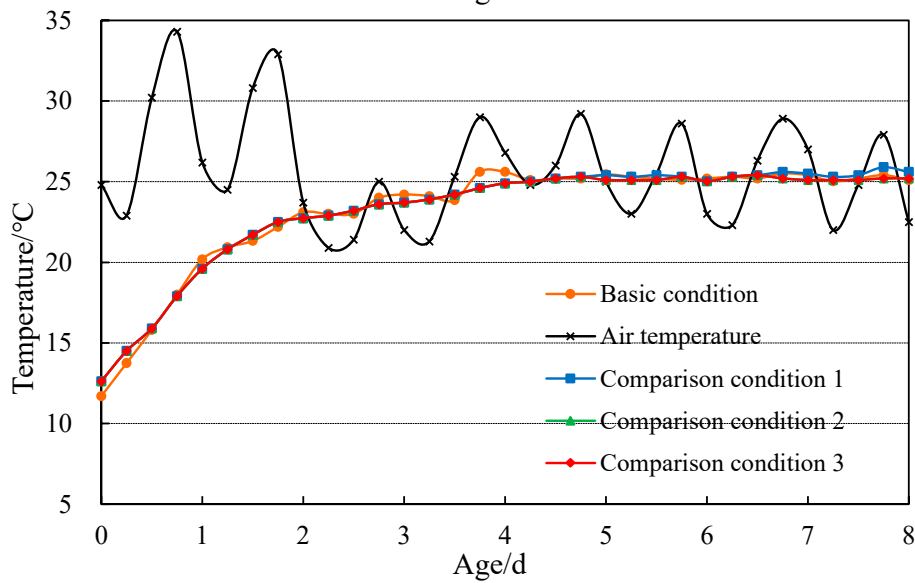
Figure 18 shows the temperature-time curves of concrete at different depths from the top surface of the pouring silo under basic working conditions and comparison working conditions 4–7. The maximum daily variation of temperature at different depths from the top surface of the pouring silo under basic working conditions and comparison working conditions 4–7 is calculated, as shown in Table 14. Figure 19 shows the temperature change rate-time curve of the concrete 10 cm away from the top of the pouring block under basic conditions and comparison conditions 4–7. From the above results, it can be seen that at the initial stage of concrete pouring, the effect of concrete curing with different water temperatures under calculation conditions is roughly the same, and the temperature control effect of the concrete surface is obvious. In the high-temperature season, considering the temperature control effect, the field-measured water temperature distribution range, and economics, it is recommended to use 22–24 °C water temperature for water curing during the daytime high-temperature period and to provide coverage with a 4-centimeter-thick polyethylene coil at night.



10 cm from the top surface



20 cm from the top surface



40 cm from the top surface

Figure 15. Cont.

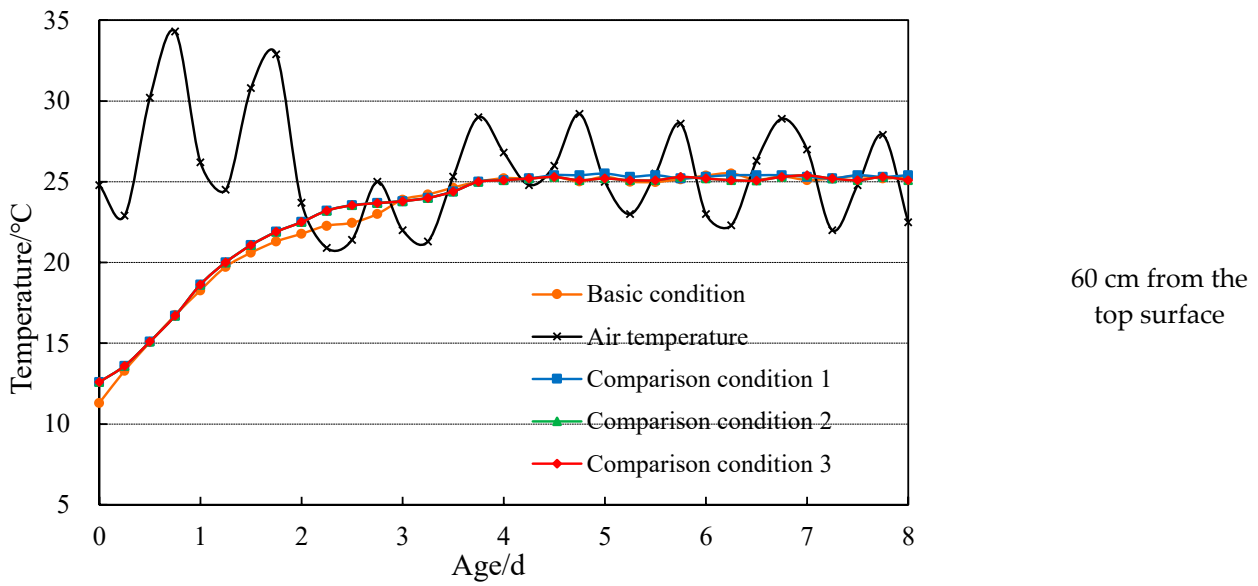


Figure 15. Temperature duration curves of concrete at different depths from the top of the pouring block under the basic conditions and comparison conditions 1–3.

Table 12. Maximum daily variation of concrete temperature at different depths from the top surface under basic conditions and comparison conditions 1–3.

Depth from the Top Surface	Basic Condition	Comparison Condition 1	Comparison Condition 2	Comparison Condition 3
10 cm	11.9 °C	10.2 °C	8.6 °C	8.0 °C
20 cm	10.2 °C	8.8 °C	7.6 °C	7.2 °C
40 cm	8.5 °C	7.0 °C	7.0 °C	7.0 °C
60 cm	7.0 °C	6.0 °C	6.0 °C	6.0 °C

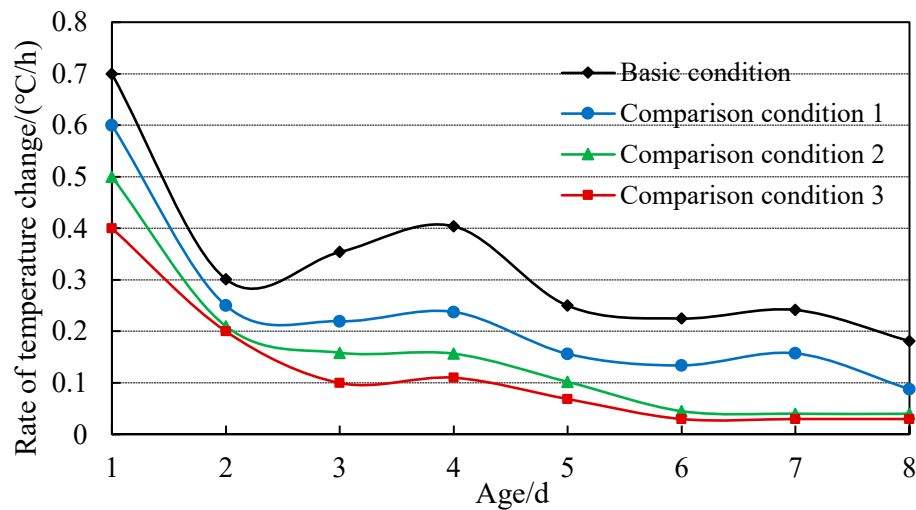
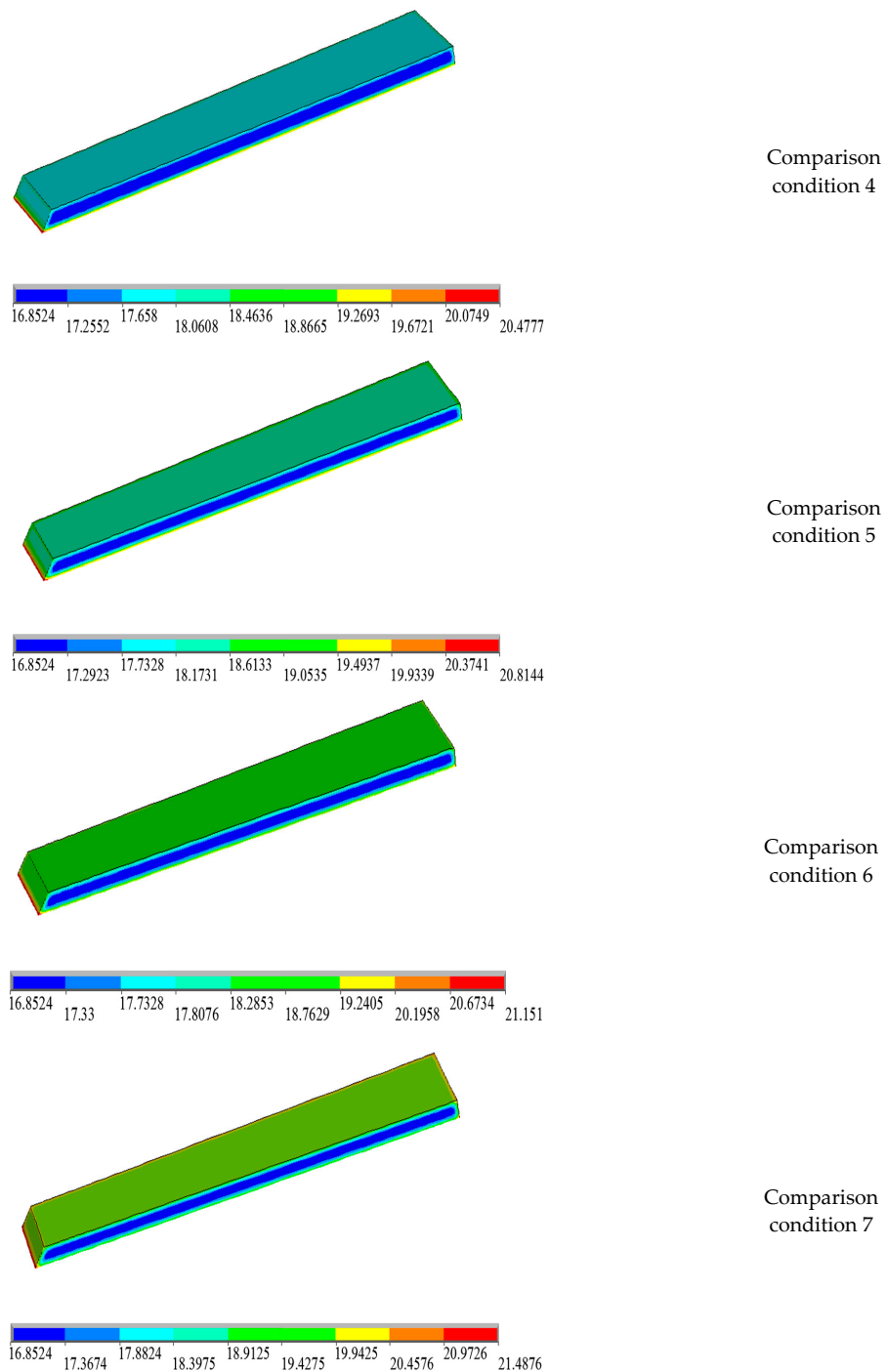


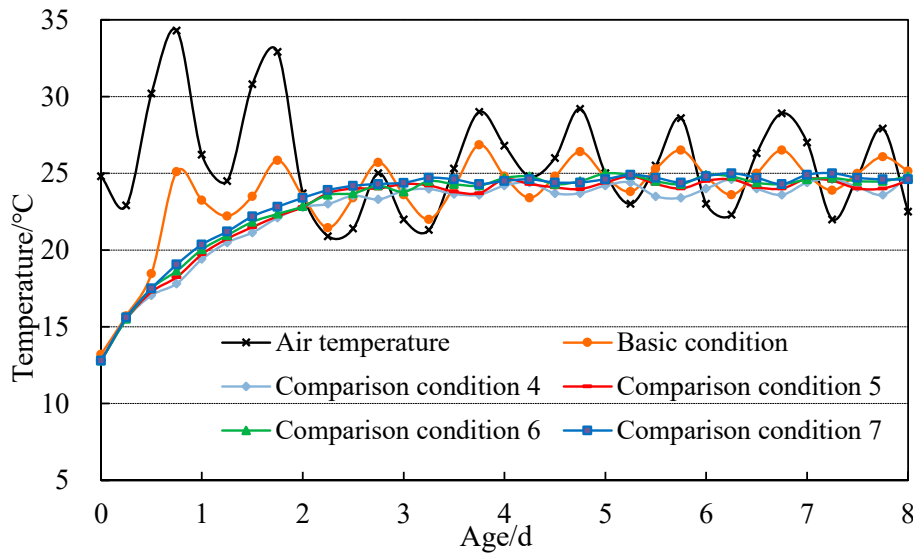
Figure 16. Duration curves of the temperature change rate of concrete under basic conditions and comparison conditions 1–3.

**Table 13.** Calculation table for different types of water temperature flow maintenance.

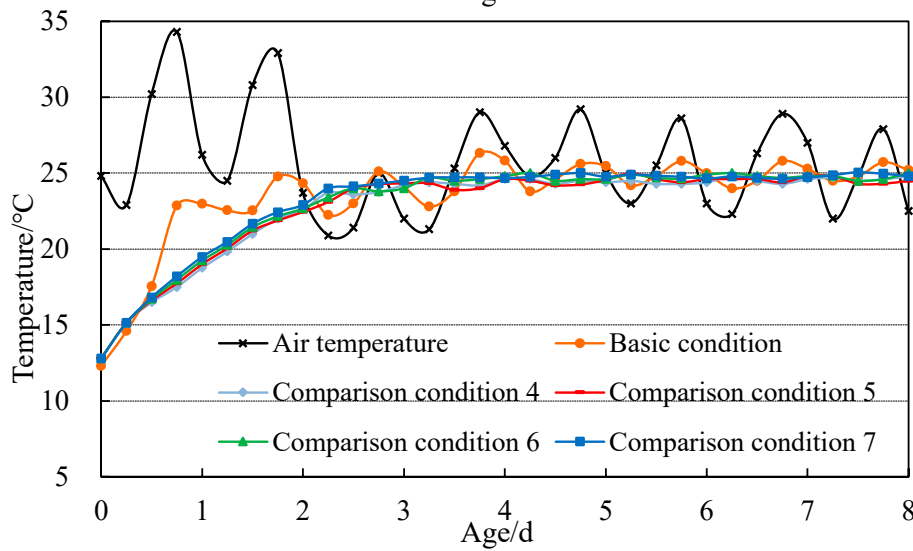
Calculation Condition	Daytime Strong Solar Radiation Period Water temperature flow maintenance	Night Polyethylene coil
Comparison condition 4	18 °C	4 cm
Comparison condition 5	20 °C	4 cm
Comparison condition 6	22 °C	4 cm
Comparison condition 7	24 °C	4 cm



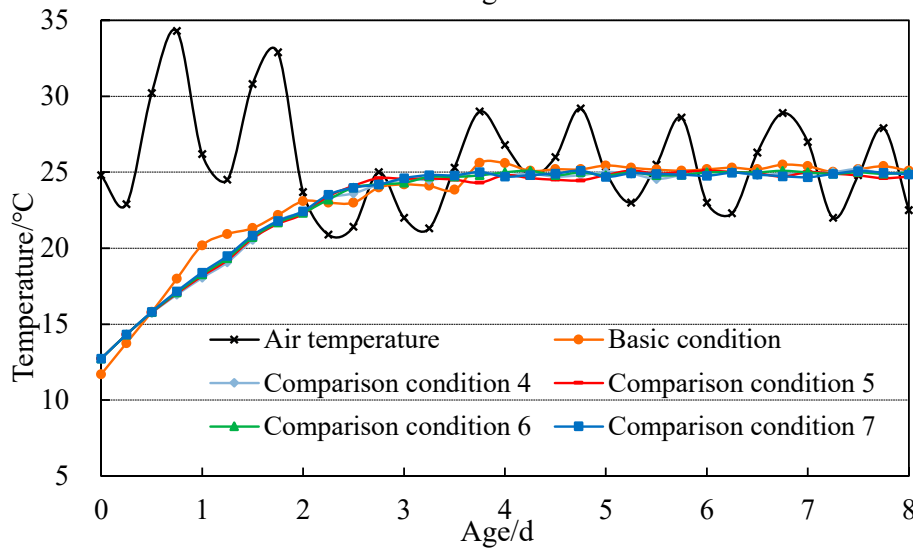
**Figure 17.** Temperature distribution cloud map of pouring blocks along the river center under basic conditions and comparison conditions 4–7.



10 cm from the top surface



20 cm from the top surface



40 cm from the top surface

Figure 18. Cont.

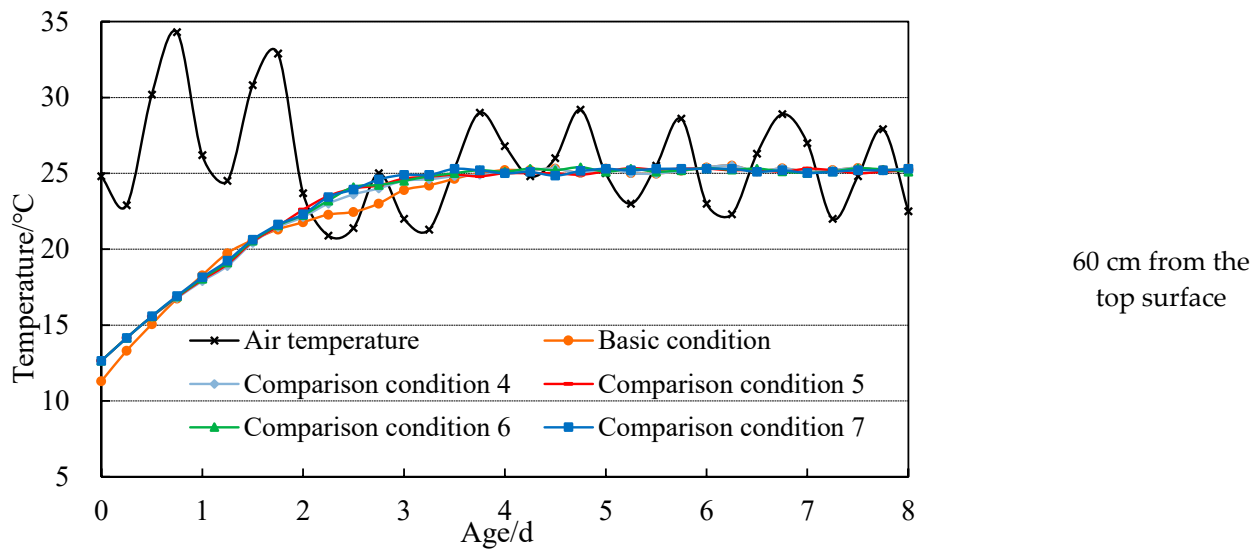


Figure 18. Temperature duration curves of concrete at different depths from the top of the pouring block under basic conditions and comparison conditions 4–7.

Table 14. Maximum daily variation of concrete temperature at different depths from the top surface under basic conditions and comparison conditions 4–7.

Depth from the Top Surface	Basic Conditions	Comparison Condition 4	Comparison Condition 5	Comparison Condition 6	Comparison Condition 7
10 cm	11.9 °C	6.6 °C	7.0 °C	7.2 °C	7.6 °C
20 cm	10.2 °C	6.0 °C	6.4 °C	6.4 °C	6.7 °C
40 cm	8.5 °C	5.3 °C	5.4 °C	5.6 °C	5.7 °C
60 cm	7.0 °C	5.2 °C	5.3 °C	5.4 °C	5.5 °C

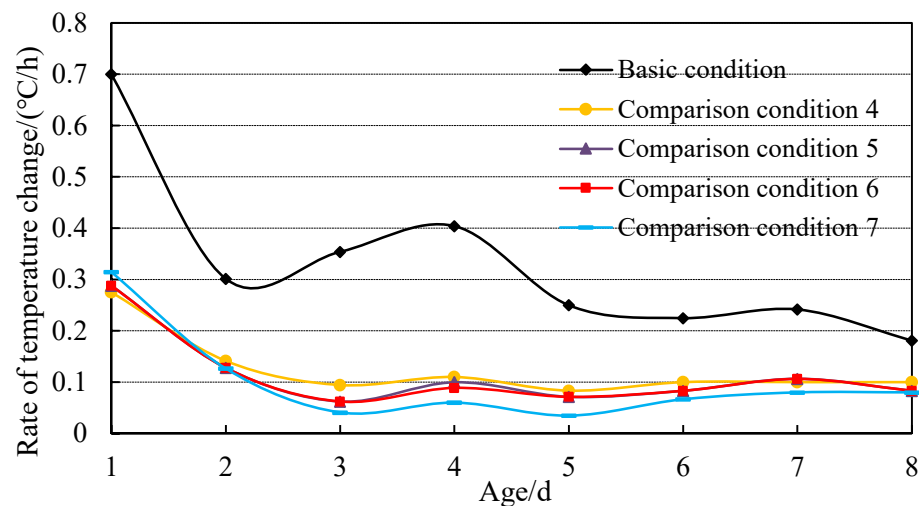


Figure 19. Duration curves of the temperature change rate of concrete under basic conditions and comparison conditions 4–7.

#### 4. Conclusions

In this study, a DTS system is applied to monitor the surface temperature gradient of concrete in real time, and a solar radiation heat monitoring test is also carried out based on the Baihetan project. Based on this, a solar radiation loading model and a finite element model of a typical pouring block are established. Combined with the measured temperature

data and different calculation conditions, the surface temperature changes of medium and low-heat concrete under solar radiation are analyzed, and the temperature control effect of surface concrete with different surface insulation measures is further analyzed. The following results can be obtained:

(1) Based on the monitoring experiment, solar radiation heat has a great influence on the temperature of low-heat concrete at different depths from the top surface, especially 10–20 cm from the top surface. With the increase in ambient temperature and sunshine, the temperature difference between the inside and outside of the concrete increases. According to the measured data, when the temperature reaches 32 °C, the temperature difference between concrete 10 cm from the top and 60 cm from the top reaches 8.3 °C.

(2) The influence depth of solar radiation heat on the temperature of medium and low-heat concrete is the same, within 40 cm from the top of the pouring block. Under intense solar radiation, the temperature variation of medium-heat concrete is more obvious than that of low-heat concrete in the same period.

(3) The low-heat concrete on the surface of a concrete block has strong sunshine in the daytime and the temperature is above 30 °C. The top surface is covered with a 4- or 5-centimeter-thick polyethylene coil, and the peak elimination effect is obvious. The maximum daily variation of concrete temperature is reduced from 12.28 °C to 8.61 °C and 8.05 °C. The maximum temperature gradient is reduced from 16.6 °C·m<sup>-1</sup> to 8.6 °C·m<sup>-1</sup> and 7.2 °C·m<sup>-1</sup>. In an environment with a daytime temperature of about 25 °C and strong sunshine, the temperature control effect of providing coverage with 2-, 4-, and 5-centimeter-thick polyethylene sheets on the top surface is not significantly different, which can effectively reduce the influence of solar radiation heat on the surface temperature of low-heat concrete.

(4) Based on the finite element calculation model of a pouring block considering solar radiation heat, the temperature control effect of the top surface of the pouring block with two kinds of heat preservation measures is calculated. The first kind of heat preservation measure involves the top surface of the pouring block being covered with 2-, 4-, and 5-centimeter-thick polyethylene coils, and the second kind of heat preservation measure involves water curing at different temperatures. The calculation results show that: (1) Under the condition of strong solar radiation heat, the top surface of the pouring silo covered with 2-centimeter-thick polyethylene coils is not enough to meet the requirements of temperature control and crack prevention for early-age concrete. Coverage with 4- and 5-centimeter-thick polyethylene coils can not only prevent the surface temperature rise caused by solar radiation heat but also reduce the temperature difference from the inside to the outside of concrete caused by a large temperature difference between day and night. Therefore, considering the weather characteristics of a high temperature, strong radiation, and a large temperature difference between day and night in the Baihetan dam, it is suggested that the top surface insulation material should be mainly 4-centimeter-thick polyethylene coils from the perspective of economic practicability and an effective temperature control effect. (2) Water curing in the range of 18–24 °C during the day and coverage with 4-centimeter-thick polyethylene coils on the top surface at night can effectively reduce the temperature difference, temperature gradient, and temperature variation range of the surface concrete and reduce the influence of solar radiation heat on the temperature effect of concrete.

Therefore, from the economic point of view and the distribution range of river water temperature, it is suggested that 22–24 °C water temperature should be used for water curing in periods of high temperatures and strong solar radiation during the day, and a 4-centimeter-thick polyethylene coil should provide coverage at night. These temperature control schemes have been applied to the Baihetan arch dam and have achieved a remarkable effect.

In future research, the temperature gradient monitoring and analysis of multiple positions in the pouring block should be further carried out, and a more reasonable and accurate simulation calculation model should be combined to realize the temperature control effect evaluation and temperature control measures implementation suggestions

under different temperature control measures and different solar radiation intensities for the low-heat concrete.

**Author Contributions:** Conceptualization, Z.L.; Methodology, H.Z.; Software, C.Z.; Validation, H.Z.; Investigation, Z.L.; Resources, F.W.; Writing—original draft, H.Z.; Writing—review & editing, C.Z. and Y.Z.; Project administration, Y.Z. All authors have read and agreed to the published version of the manuscript.

**Funding:** This research work was supported by the Youth Fund project of the National Natural Science Foundation of China (No. 52109157).

**Acknowledgments:** The authors thank the reviewers and editors for useful comments and suggestions that helped improve the paper.

**Conflicts of Interest:** The authors declare no conflict of interest.

## References

1. Liu, L.; Zhao, S.; Xin, J.; Wang, Z. Simplified Analysis of Thermal Cracks in Low-Heat Portland Cement Concrete. *Adv. Civ. Eng.* **2022**, *2022*, 7630568. [CrossRef]
2. Basoeki, M.; Koespiadi; Ekaputri, J.J. Low heat concrete hydration thermal reduction with bioconc. *IOP Conf. Ser. Mater. Sci. Eng.* **2019**, *615*, 012110. [CrossRef]
3. Fan, Q.; Li, W.; Li, X. Key construction technologies of low heat Portland cement dam concrete. *J. Hydroelectr. Eng.* **2017**, *36*, 11–17.
4. Peng, H.; Lin, P.; Xiang, Y.; Hu, J.; Yang, Z. Effects of Carbon Thin Film on Low-Heat Cement Hydration, Temperature and Strength of the Wudongde Dam Concrete. *Buildings* **2022**, *12*, 717. [CrossRef]
5. Wang, L.; Yang, H.Q.; Dong, Y.; Chen, E.; Tang, S.W. Environmental evaluation, hydration, pore structure, volume deformation and abrasion resistance of low heat Portland (LHP) cement-based materials. *J. Clean. Prod.* **2018**, *203*, 540–558. [CrossRef]
6. Zheng, Y.; Ma, M.; Zhou, J. Review of Mechanical Properties and Damage Theory of Fiber-Reinforced Low-Heat Cement Concrete. *Arab. J. Sci. Eng.* **2023**, *48*, 4175–4194. [CrossRef]
7. Mun, J.-S.; Yang, K.-H.; Kim, S.-J. Evaluation of Shrinkage and Creep Behavior of Low-Heat Cement Concrete. *J. Korea Inst. Build. Constr.* **2016**, *16*, 305–311. [CrossRef]
8. Ustabaş, İ.; Deşik, F. Transition coefficients between compressive strengths of samples with different shape and size in mass concrete and use of weight maturity method in dam construction. *Struct. Concr.* **2020**, *22*, E696–E709. [CrossRef]
9. Wang, Q.; Liu, R.; Liu, P.; Liu, C.; Sun, L.; Zhang, H. Effects of silica fume on the abrasion resistance of low-heat Portland cement concrete. *Constr. Build. Mater.* **2022**, *329*, 127165. [CrossRef]
10. Hu, Y.; Yao, Y.; Luo, R. Application of low-heat Portland cement in the abrasion resistance concrete in Xiangjiaba project. *Hydropower New Energy* **2014**, *2*, 8–42. [CrossRef]
11. Sun, M.; Hu, Z.; Shi, Y.; Song, D. Application of low-heat silicate cement in spillway tunnel engineering. *Yangtze River* **2011**, *42* (Suppl. S2), 157–159.
12. Chen, R.; Lou, X. Application of low thermal silicate cement in the diversion tunnel of Baihetan hydropower station. *Water Resour. Hydropower Eng.* **2015**, *46* (Suppl. S2), 1–4.
13. Mun, J.; Yang, K.; Kim, S. Long-Term Behavior of Low-Heat Cement Concrete under Different Curing Temperatures. *Key Eng. Mater.* **2016**, *723*, 819–823. [CrossRef]
14. Xin, J.; Zhang, G.; Jiang, X.; Chen, Z.; Qi, C.; Zhang, L.; Wang, Z.; Liu, Y. Exploring the effect of low-heat cement on early-age thermal cracking resistance of roller-compacted concrete. *J. Mater. Res. Technol.* **2022**, *21*, 4439–4451. [CrossRef]
15. Ji, T.; Ji, G.; Chen, G. Influence of low-heat Portland cement on properties of dam concrete. *J. Hydroelectr. Eng.* **2012**, *31*, 207–210.
16. Yang, H.; Wang, Y.; Zhou, S. Anti-crack performance of low-heat Portland cement concrete. *J. Wuhan Univ. Technol. Mater. Sci. Ed.* **2007**, *22*, 555–559. [CrossRef]
17. Xin, J.; Zhang, G.; Liu, Y.; Wang, Z.; Yang, N.; Wang, Y.; Mou, R.; Qiao, Y.; Wang, J.; Wu, Z. Environmental impact and thermal cracking resistance of low heat cement (LHC) and moderate heat cement (MHC) concrete at early ages. *J. Build. Eng.* **2020**, *32*, 101668. [CrossRef]
18. Shi, J.; Tan, J.; Liu, B.; Liu, Y.; Xu, H.; Wang, Z.; Xiong, T.; Shi, J. Thermal and mechanical properties of thermal energy storage lightweight aggregate mortar incorporated with phase change material. *J. Energy Storage* **2020**, *32*, 101719. [CrossRef]
19. Moelich, G.; Van Zyl, J.E.; Rabie, N.; Combrinck, R. The influence of solar radiation on plastic shrinkage cracking in concrete. *Cem. Concr. Compos.* **2021**, *123*, 104182. [CrossRef]
20. Cebeci, O.Z.; Saatci, A.M. Estimation of Evaporation from Concrete Surfaces. In Proceedings of the Third International RILEM Conference: Concrete in Hot Climates, Torquay, UK, 1992. Available online: <http://worldcat.org/isbn/0419180907> (accessed on 1 July 1992).
21. Bentz, D.P. *A Computer Model to Predict the Surface Temperature and Time-of-Wetness of Concrete Pavements and Bridge Decks*; NIST Interagency/Internal Report (NISTIR); National Institute of Standards and Technology: Gaithersburg, MD, USA, 2000. Available online: [https://tsapps.nist.gov/publication/get\\_pdf.cfm?pub\\_id=860286](https://tsapps.nist.gov/publication/get_pdf.cfm?pub_id=860286) (accessed on 1 August 2000).

22. Wang, F.; Zhang, A.; Fan, Y.; Zhou, Y.; Chen, J.; Tan, T. Temperature monitoring experiment and numerical simulation of the orifice structure in an arch dam considering solar radiation effects. *J. Civ. Struct. Health Monit.* **2023**, *13*, 523–545. [[CrossRef](#)]
23. Sheng, X.; Chen, Z.; Zheng, W.; Xu, H. Time-varying solar radiation-induced non-uniform temperature distribution of steel-concrete composite box girder-ballastless track system. *Case Stud. Therm. Eng.* **2023**, *43*, 102750. [[CrossRef](#)]
24. Chang, X.; Liu, X.; Wei, B. Temperature simulation of RCC gravity dam during construction considering solar radiation. *Eng. J. Wuhan Univ.* **2006**, *39*, 26–29.
25. Huang, D.; Huang, W. Temperature simulation computation of RCC placing face under solar radiation. *Yangtze River* **2007**, *38*, 22–25.
26. Li, B.; Wang, Z.; Jiang, Y.; Zhu, Z. Temperature control and crack prevention during construction in steep slope dams and stilling basins in high-altitude areas. *Adv. Mech. Eng.* **2018**, *10*, 1–15. [[CrossRef](#)]
27. Zhu, Z.; Liu, Y.; Tan, Y. Simulation of Temperature Field of High Arch Dams Considering Solar Radiation. *IOP Conf. Ser. Earth Environ. Sci.* **2020**, *455*, 012003. [[CrossRef](#)]
28. Ren, Z.; Hu, S.; Ding, Q. Research on the effect of solar radiation model on temperature field of concrete-filled steel tube pier. *Eng. Mech.* **2010**, *27*, 246–250.
29. Larsson, O.; Thelander, S. Estimating extreme values of thermal gradients in concrete structures. *Mater. Struct.* **2011**, *44*, 1491–1500. [[CrossRef](#)]
30. Zhou, Y.; Zhou, J.; Huang, Y.; Zhou, S.; Li, J. Monitoring of temperature gradient on concrete surface by distributed optical fiber and feedback analysis. *J. Yangtze River Sci. Res. Inst.* **2012**, *29*, 42–45.
31. Su, W.; Dai, J.; Li, N.; Huang, D. Research on temperature field of concrete guide wall based on different solar radiation models. *Water Power* **2013**, *39*, 32–36.
32. Zhou, G.; Yi, T. Thermal load in large-scale bridges: A state-of-the-art review. *Int. J. Distrib. Sens. Netw.* **2013**, *9*, 1–16. [[CrossRef](#)]
33. Zhao, R.; Wang, Y. Studies on temperature field boundary conditions for concrete box-girder bridges under solar radiation. *China J. Highw. Transp.* **2016**, *29*, 52–61.
34. Soltani, N.; Alembagheri, M.; Khaneghahi, M. Risk-based probabilistic thermal-stress analysis of concrete arch dams. *Front. Struct. Civ. Eng.* **2019**, *13*, 1007–1019. [[CrossRef](#)]
35. Castilho, E.; Schlar, N.; Tiago, C.; Farinha, M. FEA model for the simulation of the hydration process and temperature evolution during the concreting of an arch dam. *Eng. Struct.* **2018**, *174*, 165–177. [[CrossRef](#)]
36. Liang, Z.; Zhao, C.; Zhou, H.; Liu, Q.; Zhou, Y. Error correction of temperature measurement data obtained from an embedded bifilar optical fiber network in concrete dams. *Measurement* **2019**, *148*, 106903. [[CrossRef](#)]
37. De Jong, S.A.P.; Slingerland, J.D.; Van de Giesen, N.C. Fiber optic distributed temperature sensing for the determination of air temperature. *Atmos. Meas. Tech.* **2015**, *8*, 335–339. [[CrossRef](#)]
38. Pei, H.; Teng, J.; Tin, J.; Chen, R. A review of previous studies on the applications of optical fiber sensors in geotechnical health monitoring. *Measurement* **2014**, *58*, 207–214. [[CrossRef](#)]
39. Leung, C.K.Y.; Wan, K.T.; Daniele, I.; Bao, X.; Habel, W.; Zhou, Z.; Ou, J.; Ghandehari, M.; Wu, H.C.; Imai, M. Review: Optical fiber sensors for civil engineering applications. *Mater. Struct.* **2015**, *48*, 871–906. [[CrossRef](#)]
40. Zhou, H.; Pan, Z.; Liang, Z.; Zhao, C.; Zhou, Y.; Wang, F. Temperature field reconstruction of concrete dams based on distributed optical fiber monitoring data. *KSCE J. Civ. Eng.* **2019**, *23*, 1911–1922. [[CrossRef](#)]
41. Zhou, Y.; Liang, C.; Wang, F.; Zhao, C.; Zhang, A.; Tan, T.; Gong, P. Field test and numerical simulation of the thermal insulation effect of concrete pouring block surface based on DTS. *Constr. Build. Mater.* **2022**, *343*, 128022. [[CrossRef](#)]
42. Antunes, P.; Lima, H.; Varum, H.; André, P. Optical fiber sensors for static and dynamic health monitoring of civil engineering infrastructures: Abode wall case study. *Measurement* **2012**, *45*, 1695–1705. [[CrossRef](#)]
43. Zhou, H.; Zhou, Y.; Zhao, C.; Wang, F.; Liang, Z. Feedback Design of Temperature Control Measures for Concrete Dams based on Real-Time Temperature Monitoring and Construction Process Simulation. *KSCE J. Civ. Eng.* **2018**, *22*, 1584–1592. [[CrossRef](#)]
44. Zhu, B. *Thermal Stresses and Temperature Control of Mass Concrete*; China Water Power Press: Beijing, China, 2012.
45. Zhou, H.; Zhou, Y.; Zhao, C.; Liang, Z. Optimization of the temperature control scheme for roller compacted concrete dams based on finite element and sensitivity analysis methods. *Civ. Eng. J.* **2016**, *25*. [[CrossRef](#)]
46. Wang, F.; Zhou, Y.; Zhao, C.; Zhou, H.; Wang, F. Inversion method of mass concrete thermal parameters considering measuring point sensitivity. *J. Hydroelectr. Eng.* **2017**, *36*, 95–104.
47. Wang, F.; Zhou, H.; Zhou, Y.; Zhao, C.; Seman Ebrahim, A.; Gong, P. Thermal Parameters Inversion Method for Concrete Dam Based on Optimal Temperature Measuring Point Selecting. *Math. Probl. Eng.* **2022**, *2022*, 4677344. [[CrossRef](#)]

**Disclaimer/Publisher’s Note:** The statements, opinions and data contained in all publications are solely those of the individual author(s) and contributor(s) and not of MDPI and/or the editor(s). MDPI and/or the editor(s) disclaim responsibility for any injury to people or property resulting from any ideas, methods, instructions or products referred to in the content.